AIAA JOURNAL
Vol. 60, No. 11, November 2022

Spatial Input–Output Analysis of Actuated Turbulent Boundary Layers

Chang Liu* and Igal Gluzman†
Johns Hopkins University, Baltimore, Maryland 21218
Mitchell Lozier,‡ Samaresh Midya,‡ Stanislav Gordeyev,§ and Flint O. Thomas¶
University of Notre Dame, Notre Dame, Indiana 46556
and
Dennice F. Gayme**
Johns Hopkins University, Baltimore, Maryland 21218

https://doi.org/10.2514/1.J061706

This paper develops a spatial input–output approach to investigate the dynamics of a turbulent boundary layer subject to a localized single frequency excitation. One-way spatial integration is used to reformulate the problem in terms of spatial evolution equations. The associated input-output operator is then used to examine the effect of localized periodic actuation at a given temporal frequency, based on an experimental setup in which an active large scale structure is introduced into the outer layer of a turbulent boundary layer. First, the large-scale structures associated with the phase-locked modal velocity field obtained from spatial input–output analysis are shown to closely match those computed based on hot-wire measurements. The approach is then used to further investigate the response of the boundary layer to the synthetically generated large-scale structures. A quadrant trajectory analysis indicates that the spatial input–output response produces shear stress distributions consistent with those in canonical wall-bounded turbulent flows in terms of both the order and types of events observed. The expected correspondence between the dominance of different quadrant behavior and actuation frequency is also observed. These results highlight the promise of a spatial input–output framework for analyzing the formation and streamwise evolution of structures in actuated wall-bounded turbulent flows.

Nomenclature

$\check{\boldsymbol{A}}_S$	=	spatial state evolution operator
$\check{\boldsymbol{B}}_S$	=	input operator for spatial input-output analysis
$\check{\boldsymbol{C}}_S$	=	output operator for spatial input-output analysis
$\boldsymbol{e}_x$	=	streamwise unit vector
F_0	=	magnitude of body force
f_x	=	streamwise component of the body force modeling plasma actuation
$\mathbb{I}m[\cdot]$	=	imaginary part of argument
i	=	imaginary unit, equal to $\sqrt{-1}$
k_x	=	streamwise wave number
k_z	=	spanwise wave number
M	=	$\nu(\partial_y^2 - k_z^2) - \eta + \mathrm{i}\omega$ (employed to simplify notation)
p	=	pressure fluctuation
p_{tot}	=	pressure
$\bar{p}$	=	time-averaged pressure
$\check{\boldsymbol{q}}_S$	=	state variable for spatial input–output system
$\mathbb{R}e[\cdot]$	=	real part of argument
Re_τ	=	friction Reynolds number
T	=	final time for time averaging
t	=	time
u	=	streamwise velocity fluctuation from the model or instantaneous streamwise velocity from the experiments
u_s	=	downstream evolution of phase-locked streamwise velocity
u_{tot}	=	streamwise velocity
u_τ	=	friction velocity
v_s	=	downstream evolution of phase-locked wall-normal velocity
$\bar{u}$	=	streamwise component of the time-averaged turbulent mean velocity
$\tilde{u}$	=	phase-locked modal streamwise velocity
u'	=	residual fluctuating turbulent streamwise velocity
$\boldsymbol{V}$	=	matrix containing eigenvectors of $\check{\boldsymbol{A}}_S$
v	=	wall-normal velocity fluctuation
v_{tot}	=	wall-normal velocity
$\check{v}_x$	=	$\partial\check{v}/\partial x$
w	=	spanwise velocity fluctuation
w_{tot}	=	spanwise velocity
$\check{w}_x$	=	$\partial\check{w}/\partial x$
x	=	streamwise location
x_m	=	streamwise location of measurement
x_0	=	streamwise location of forcing
y	=	wall-normal location
y_f	=	wall-normal location of the center of a body force
y_p	=	wall-normal location of the plasma actuator plate
z	=	spanwise location
$\delta(\cdot)$	=	Dirac delta function
δ_v	=	inner unit length scale
δ_{99}	=	boundary-layer thickness
δ_{99}^+	=	boundary-layer thickness in inner units
η	=	temporal growth rate
$\boldsymbol{\Lambda}$	=	diagonal matrix containing eigenvalues of $\check{\boldsymbol{A}}_S$
λ_x	=	streamwise wavelength
λ_z	=	spanwise wavelength

Presented as Paper 2021-2873 at the AIAA Aviation 2021 Forum, Virtual Event, August 2–6, 2021; received 4 February 2022; revision received 25 June 2022; accepted for publication 12 July 2022; published online 23 August 2022.

*Graduate Student, Department of Mechanical Engineering; currently Postdoctoral Scholar, Department of Physics, University of California, Berkeley, CA; cliu124@alumni.jh.edu (Corresponding Author).
†Postdoctoral Fellow, Department of Mechanical Engineering; currently Postdoctoral Research Associate, Department of Aerospace and Mechanical Engineering, University of Notre Dame, Notre Dame, IN.
‡Graduate Student, Department of Aerospace and Mechanical Engineering. Student Member AIAA.
§Associate Professor, Department of Aerospace and Mechanical Engineering. Associate Fellow AIAA.
¶Professor, Department of Aerospace and Mechanical Engineering. Associate Fellow AIAA.
**Associate Professor, Department of Mechanical Engineering.

ν = kinematic viscosity
ρ = density
σ_p = standard deviation of Gaussian function of body force
$\bar{\tau}_w$ = time-averaged mean shear stress at wall
ϕ = phase
ϕ_0 = initial phase of body force
$\boldsymbol{\Psi}$ = operator mapping state $\boldsymbol{q}_S$ at x equal to x_0 to $\boldsymbol{q}_S$ at x equal to x_m at the same frequency–wave number pair (ω, k_z)
ψ = a nominal variable
ω = temporal frequency
ω_z = spanwise vorticity fluctuation
$\omega_{z,s}$ = downstream evolution of phase-locked spanwise vorticity
$\mathbf{0}$ = zero matrix
$\bar{(\cdot)}$ = time-averaging operation
$(\cdot)^+$ = variable normalized by the inner units: δ_v and u_τ
$\check{(\cdot)}$ = Laplace transform in time domain and Fourier transform in spanwise domain

I. Introduction

LARGE-SCALE structures in turbulent boundary layers (TBL) are known to contribute significantly to the turbulent kinetic energy and Reynolds stress production [1,2], which influence the near-wall small-scale structures [3–5] and local skin friction [6]. This influence of the large-scale structures on the TBL dynamics has been shown to increase with Reynolds number [7]. Large-scale structures can also be manipulated to change the properties of the boundary layer, for example, to reduce drag in a high Reynolds number TBL [8]; see, for example, the review in Ref. [9]. Therefore, understanding their dynamics and interactions with the overall TBL can provide insight into the underlying physics.

The dynamics of large-scale structures can be studied by analyzing the flow response to an external large-scale perturbation. Single harmonic perturbations provide a particularly attractive approach to tracking the linear response of the TBL at the same frequency through phase-locked analysis. Investigating these types of actuated flows dates back to the work of Hussain and Reynolds [10,11], in which a thin vibrating ribbon near the wall is used to introduce perturbations into turbulent channel flow. They analyzed the experimental results by introducing a triple decomposition of the instantaneous velocity into a temporal mean, phase-locked harmonic perturbations (organized waves), and the remaining turbulence. Periodic perturbations have also been experimentally introduced into a TBL through a dynamic (temporally oscillating) roughness, which provides a reference phase to isolate the synthetic large-scale and small-scale flow structures [12–15]. The introduced periodic perturbation is shown to alter the phase relation between large and small scales and the associated modulation coefficient in a quasi-deterministic manner [16]. Temporal periodic perturbations can be also introduced by a wall jet [17,18] or a wall-mounted piezoelectric actuator [19–21]. Ranade et al. [22] introduced the perturbation outside (above) the boundary layer instead of at the wall. Their results support the existence of a critical layer inside the wake region that is responsible for the amplified level of turbulence in that region. Lozier et al. [23–25] similarly introduced large-scale perturbations in the outer region of the boundary layer through a dielectric barrier discharge (DBD) plasma actuator. They then performed a triple decomposition with a phase-locked velocity to obtain synthetic large-scale structures and investigate their interactions with the residual turbulence.

In the afore mentioned experiments, the dominant temporal frequency of the perturbation determines the frequency for the velocity decomposition and acts as an input in models of the phenomena. However, there remains a lack of understanding regarding a suitable choice of the streamwise wave number to, for example, specify a convective velocity, or for use in input–output based techniques that decompose the flow into a superposition over these wave numbers. As such, there have been a number of methods used to determine the streamwise wave number of interest. Jacobi and McKeon [13] compared the phase-locked velocity measured in a TBL perturbed by dynamic roughness with predictions from resolvent analysis [26]. They determined a streamwise wave number for modeling synthetic large-scale structures based on a least-squares fit over several downstream measurements. This method led to good agreement with the experimental data for that particular case; however, in general, spatially localized perturbations are known to break the shift invariance in the streamwise direction assumed in the resolvent model [13,27]. Therefore, the streamwise variation may be more accurately characterized by a complex wave number that would also capture downstream growth or decay [13,27]. In addition, a single frequency perturbation has been shown to be associated with a broad band of streamwise wave numbers [27]. For example, the single frequency that is introduced through the perturbation will result in different streamwise wave numbers at different wall-normal heights depending on the local mean velocity [13,27]. Therefore, limiting the analysis to a single streamwise wave number may restrict the range of behaviors that can be studied.

In this work, we develop a spatial input–output analysis approach that does not require specification of a single streamwise wave number. Our approach uses the integration method of Towne and Colonius [28] to reformulate the problem in terms of well-posed and exact one-way spatial evolution equations that inherently represent the behavior across the streamwise spectra. This reformulation also results in a natural embedding of a wall-normal dependent phase speed that enables specification of a local (wall-normal direction dependent) convective velocity. We apply the proposed approach to analyze the phase-locked velocity and evolution of large-scale structures in a low Reynolds number TBL, where a synthetic large-scale structure is introduced through a spanwise-uniform DBD plasma actuator based on the experimental setup in Refs. [23–25]. We first demonstrate the ability to produce phase-locked velocities with large-scale structures reminiscent of those obtained by experimental measurements employing hot-wire anemometry and a phase-locked analysis. Both the theory and experiments indicate that the actuated large-scale structures become more inclined toward the wall as they propagate downstream, which is indicative of the changes in phase speed with distance from the wall. Quadrant analysis [29,30] indicates that the shear stress distribution of the spatially evolving flowfield shows an ordering (spatial progression of quadrant behaviors) consistent with that observed in turbulent pipe flows [31].

The last part of this work exploits the analytical structure of the approach to take some steps toward characterizing the effect of varying the height and actuation frequency, thereby addressing a gap in the literature that has thus far focused on periodic perturbations injected at the wall [10,11,13,17–21,27,32–34] and perturbations introduced in the outer layer [22–25]. Our studies indicate that the actuation frequency influences the characteristic streamwise length scale and that the response to higher-frequency actuation decays faster in the downstream direction. The ordering of the shear stress patterns from quadrant analysis is found to be independent of actuator height. The perturbation location instead determines a phase speed for flow structures associated with the local mean velocity at that height. In contrast, changes in actuation frequency affect the most commonly occurring shear stress patterns in a manner consistent with canonical wall-bounded turbulence. These results support the notion that synthetic large-scale structures interact with the TBL in a manner consistent with naturally occurring large-scale structures. They also highlight the promise of combining such an analysis with experimental studies to provide further insight into scale interactions in the TBL.

The remainder of this paper is organized as follows. Section II describes the spatial input–output analysis framework. In Sec. III, we present the experimental setup of interest and compare results obtained from a spatial input–output analysis using a model of the experimental actuation with the experimentally obtained data. Section IV employs spatial input–output analysis to analyze the downstream evolution of actuated large-scale structures as well as the influence of actuation frequency and wall-normal height on the actuated large-scale structures. Section V concludes this paper.

II. Spatial Input–Output Analysis of Actuated Turbulent Boundary Layer

We consider an incompressible zero-pressure-gradient TBL, where x, y, z are the streamwise, wall-normal, and spanwise directions, respectively. To approximate boundary-layer flow, we invoke the quasi-parallel assumption that the streamwise variation of the mean velocity is negligible, which is quantitatively shown to be a reasonable assumption by spatio-temporal measurement in Ref. [27]. We decompose the velocity field, $\boldsymbol{u}_{\text{tot}} = [\,u_{\text{tot}} \quad v_{\text{tot}} \quad w_{\text{tot}}\,]^{\text{T}}$, and the pressure field p_{tot} into mean and fluctuating quantities $\boldsymbol{u}_{\text{tot}} = \bar{u}(y)\boldsymbol{e}_x + \boldsymbol{u}$ and $p_{\text{tot}} = \bar{p} + p$, where $^{\text{T}}$ denotes the transpose, $\boldsymbol{e}_x$ denotes the streamwise unit vector, and overbars represent time-averaged quantities, $\bar{\phi} = \lim_{T\to\infty} \frac{1}{T}\int_0^T \phi(t)\,\mathrm{d}t$.

We are interested in the flow response of the TBL subject to a localized temporally harmonic oscillation at a fixed frequency applied using a spanwise uniform DBD plasma actuator. We model the effect of this plasma actuation as a streamwise body force $f_x\boldsymbol{e}_x$ and neglect any induced body forces in the wall-normal or spanwise directions. The use of this type of model is supported by the observation that plasma-induced body force typically shows a much smaller wall-normal forcing than streamwise forcing [35]. This forcing is localized; in other words, applied at a particular wall-normal and streamwise location as illustrated in Fig. 1. The form of the forcing prescribed for this study is described in detail in Sec. III.B.

The dynamics of the forced fluctuations $\boldsymbol{u}$ and p linearized around the turbulent mean velocity are governed by

$$\partial_t \boldsymbol{u} + \bar{u}\partial_x \boldsymbol{u} + v\frac{d\bar{u}}{dy}\boldsymbol{e}_x + \frac{\nabla p}{\rho} - \nu\nabla^2\boldsymbol{u} = f_x\boldsymbol{e}_x \tag{1a}$$

$$\nabla\cdot\boldsymbol{u} = 0 \tag{1b}$$

Here, ρ is the density of the fluid, and ν is kinematic viscosity. The friction Reynolds number is defined as $Re_\tau := \delta_{99}u_\tau/\nu$, where δ_{99} is the boundary-layer thickness and the friction velocity is defined as $u_\tau \equiv \sqrt{\bar{\tau}_{\text{w}}/\rho}$, where $\bar{\tau}_{\text{w}}$ is the time-averaged mean shear stress at the wall. We denote the velocity normalized by the friction velocity with a superscript$^+$; in other words, $u^+ = u/u_\tau$. We also use superscript$^+$ to denote the length normalized by the inner unit length scale $\delta_v := \nu/u_\tau$ and the time normalized by δ_v/u_τ; i.e., $y^+ = y/\delta_v$ and $t^+ = tu_\tau/\delta_v$.

We next derive a spatial mapping operator to obtain the spatial input–output system by assuming solutions of the form

$$\psi(x, y, z, t) = \check{\psi}(x, y; \omega, \eta, k_z)\mathrm{e}^{\mathrm{i}(k_z z - \omega t)}\mathrm{e}^{\eta t} \tag{2}$$

where $k_z = 2\pi/\lambda_z$ is spanwise wave number and $\mathrm{i} = \sqrt{-1}$ is the imaginary unit; η and ω, respectively, denote temporal growth rate and frequency; note η is introduced here for partitioning the upstream and downstream modes following Towne and Colonius [28] based on Briggs's [36] criteria. These assumptions allow us to rewrite Eq. (1) as

$$\frac{\partial}{\partial x}\check{\boldsymbol{q}}_S = \check{\boldsymbol{A}}_S\check{\boldsymbol{q}}_S + \check{\boldsymbol{B}}_{S,x}\check{f}_x \tag{3}$$

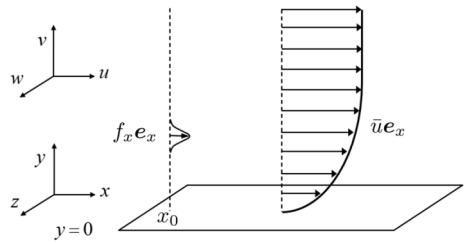

Fig. 1 Illustration of spatially localized actuation applied to a turbulent boundary layer.

where $\check{\boldsymbol{q}}_S := \left[\check{u}\ \ \check{v}\ \ \check{v}_x\ \ \check{w}\ \ \check{w}_x\ \ \check{p}/\rho\right]^{\text{T}}$, $\check{v}_x := (\partial\check{v}/\partial x)$, $\check{w}_x := (\partial\check{w}/\partial x)$, and the operators $\check{\boldsymbol{A}}_S$ and $\check{\boldsymbol{B}}_{S,x}$ are, respectively, defined as

$$\check{\boldsymbol{A}}_S(y;\omega,\eta,k_z) := \begin{bmatrix} 0 & -\partial_y & 0 & -\mathrm{i}k_z & 0 & 0 \\ 0 & 0 & 1 & 0 & 0 & 0 \\ 0 & -M/\nu & \bar{u}/\nu & 0 & 0 & \partial_y/\nu \\ 0 & 0 & 0 & 0 & 1 & 0 \\ 0 & 0 & 0 & -M/\nu & \bar{u}/\nu & \mathrm{i}k_z/\nu \\ M & -\dfrac{d\bar{u}}{dy} + \bar{u}\partial_y & -\nu\partial_y & \mathrm{i}k_z\bar{u} & -\mathrm{i}k_z\nu & 0 \end{bmatrix},$$

$$\check{\boldsymbol{B}}_{S,x} := \begin{bmatrix} 0 \\ 0 \\ 0 \\ 0 \\ 0 \\ 1 \end{bmatrix} \tag{4}$$

with

$$M := \nu(\partial_y^2 - k_z^2) - \eta + \mathrm{i}\omega \tag{5}$$

An operator similar to $\check{\boldsymbol{A}}_S$ in Eq. (4) was previously defined by Schmid and Henningson [see Ref. [37], Eqs. (7.110–7.111)]. We impose boundary conditions of the form

$$\check{u}(y=0) = \check{u}(y=\infty) = 0 \tag{6a}$$

and

$$\check{v}(y=0) = \check{v}(y=\infty) = 0 \tag{6b}$$

$$\check{w}(y=0) = \check{w}(y=\infty) = 0 \tag{6c}$$

which correspond to no-slip at the wall and no fluctuations at the freestream location.

To obtain the solution to Eq. (3), we need to first identify the upstream and downstream modes contained in $\check{\boldsymbol{A}}_S(y;\omega,\eta=0,k_z)$ to eliminate numerical instabilities associated with upstream decaying modes growing in the downstream direction. Here, we implement the one-way spatial equation [28] to explicitly identify upstream modes based on Briggs's [36] criteria; see, for example, Refs. [28,36,38] and [39]'s Sec. III.C. Following Towne and Colonius [28], we identify the eigenvalue associated with $\mathrm{i}k_x(\omega,\eta=0,k_z)$ of $\check{\boldsymbol{A}}_S(y;\omega,\eta=0,k_z)$ by tracking the eigenvalues $\mathrm{i}k_x(\omega,\eta,k_z)$ of $\check{\boldsymbol{A}}_S(y;\omega,\eta,k_z)$ as a function of η. This mode $k_x(\omega,\eta=0,k_z)$ is propagating downstream if

$$\lim_{\eta\to+\infty}\mathbb{I}\mathrm{m}[k_x(\omega,\eta,k_z)] = +\infty \tag{7}$$

and propagating upstream if

$$\lim_{\eta\to+\infty}\mathbb{I}\mathrm{m}[k_x(\omega,\eta,k_z)] = -\infty \tag{8}$$

where $\mathbb{I}\mathrm{m}[\cdot]$ represents the imaginary part of the argument. We then perform an eigenvalue decomposition,

$$\check{\boldsymbol{A}}_S(y;\omega,\eta=0,k_z) = \boldsymbol{V}\boldsymbol{\Lambda}\boldsymbol{V}^{-1} \tag{9}$$

where the diagonal elements of the diagonal matrix $\boldsymbol{\Lambda}$ and matrix $\boldsymbol{V}$, respectively, contain the eigenvalues and eigenvectors of $\check{\boldsymbol{A}}_S(y;\omega,\eta=0,k_z)$. We then eliminate the upstream modes by defining an x dependent matrix $\boldsymbol{D}$ as

$$\boldsymbol{D}_{ii}(x) = \begin{cases} e^{\boldsymbol{\Lambda}_{ii}x}, & \text{if } \boldsymbol{\Lambda}_{ii} \text{ is an eigenvalue corresponding to a downstream mode,} \\ 0, & \text{if } \boldsymbol{\Lambda}_{ii} \text{ is an eigenvalue corresponding to an upstream mode} \end{cases} \tag{10}$$

where the subscript ii represents the ith diagonal element of the matrix $\boldsymbol{D}$ or $\boldsymbol{\Lambda}$. The operator mapping the state $\boldsymbol{q}_S(x_0, y; \omega, k_z)$ at $x = x_0$ to the state $\boldsymbol{q}_S(x_m, y; \omega, k_z)$ at another downstream location $x = x_m$ under the same spatio-temporal wave number–frequency pair (ω, k_z), in other words, $\boldsymbol{q}_S(x_m, y; \omega, k_z) = \check{\boldsymbol{\Psi}}(x_m, x_0, y; \omega, k_z)\boldsymbol{q}_S(x_0, y; \omega, k_z)$, is then given by

$$\check{\boldsymbol{\Psi}}(x_m, x_0, y; \omega, k_z) \coloneqq \boldsymbol{V}\boldsymbol{D}(x_m - x_0)\boldsymbol{V}^{-1} \tag{11}$$

Using Eq. (11), we can obtain the state response $\check{\boldsymbol{q}}_S(x_m, y; \omega, k_z)$ at the frequency–wave number pair (ω, k_z) and downstream location x_m due to an input forcing function $\check{f}_x(x, y; \omega, k_z)$ with $\check{\boldsymbol{q}}_S(x_0, y; \omega, k_z) = 0$ as

$$\check{\boldsymbol{q}}_S(x_m, y; \omega, k_z) = \int_{x_0}^{x_m} \check{\boldsymbol{\Psi}}(x_m, x, y; \omega, k_z)\check{\boldsymbol{B}}_{S,x}\check{f}_x(x, y; \omega, k_z)\,\mathrm{d}x \tag{12}$$

With the additional definition of an output operator $\check{\boldsymbol{C}}$, we can obtain the response of an output variable $\check{\boldsymbol{\phi}}(x_m, y; \omega, k_z)$ for a given (ω, k_z) pair and downstream location x_m:

$$\check{\boldsymbol{\phi}}(x_m, y; \omega, k_z) = \check{\boldsymbol{C}}\,\check{\boldsymbol{q}}_S(x_m, y; \omega, k_z). \tag{13}$$

The formulation here is general for a wide range of k_z that can be determined based on actuator geometry, while we focus on the case $k_z = 0$ representing spanwise uniform actuation corresponding to the experimental setup of interest in this paper.

A. Numerical Method

We compute the spatial mapping matrix associated with the operator in (11) by first discretizing the operators in Eq. (4) using the Chebyshev differential matrices generated by the MATLAB® routines of Weideman and Reddy [40]. The mean profile $\bar{u}$ employed in this work is the asymptotic consistent TBL profile obtained from Monkewitz et al. [41] as detailed in Appendix A. This profile was also used by Cossu et al. [42] and are validated to be the same as the mean profile at $Re_\tau = 690$ obtained from directnumerical simulations [43,44]. The numerical implementation of the spatial framework is validated against the results of the spatial eigenvalue problem in Schmid and Henningson ([37], see Fig. 7.18). We implement algebraic stretching following their approach (also see Ref. [37]'s Eqs. (A.53–A.54)], and this stretched grid is validated against eigenvalue results for the Blasius boundary layer (see Ref. [37]'s Table A.4). We use $N_y = 82$ grid points in the range $y^+ \in [0,1690]$ with half of the grid points in the range of $y^+ \in [0,345]$. This resolution was deemed sufficient by verifying that the relative difference between the results reported and those obtained when the number of grid points is increased to $N_y = 122$ is less than 1%. We identify upstream and downstream modes in Eqs. (7) and (8) through the eigenshuffle function in MATLAB [45], which tracks the variation of each eigenvalue numerically based on its continuity with varying parameter η. This numerical method is selected because analytical tracking is typically challenging; see, for example, the work of Alves et al. [46]. For results reported in this work, we use 60 logarithmically spaced values in the range $\eta^+ \in [10^{-3}, 10]$ to approximate $\eta \to \infty$ in Eqs. (7) and (8). We verified that this is sufficient by checking that the results do not change if we increase this to 90 logarithmically spaced values in the range $\eta^+ \in [10^{-4}, 10^2]$. These two grids on η^+ also give the same eigenvalue of the operator $\check{\boldsymbol{A}}_S(y; \omega, \eta = 0, k_z)$ associated with the largest real part for the set of downstream eigenmodes.

III. Comparison with Experimental Results

In this section, we compare the large-scale structures from the model with those obtained from experimental measurements. We first describe the experimental setup in Sec. III.A. Then, in Sec. III.B, we describe the model calibration and provide a comparison between the phase-locked velocity obtained through the analytical approach and the experimental results.

A. Experimental Setup and Phase-Locked Decomposition

The experiments are performed in one of the low-turbulence, subsonic, in-draft wind tunnels located at the Hessert Laboratory for Aerospace Research at the University of Notre Dame. The wind tunnel has an inlet contraction ratio of 6:1 and a series of 12 turbulence-management screens in front of the inlet to achieve tunnel freestream turbulence levels of less than 0.1% (0.06% for frequencies above 10 Hz). Experiments are performed in a test section that is 0.610 m square in cross-section and 1.83 m in length. A schematic of the full experimental setup is shown in Fig. 2.

For this study, a 2-m-long boundary-layer development plate with a distributed roughness element attached to the leading edge is installed in the central height of the tunnel test section. The leading edge of the boundary-layer development plate is aligned with the test section inlet, while its trailing edge extends into the diffuser. The inlet section of the diffuser matches the test section so that approximately 17 cm of the boundary-layer development plate is inside the diffuser; this is not expected to influence the development of the TBL within the test section. A constant temperature anemometer with a single boundary-layer hot-wire probe (Dantec 55P15) with diameter 5 μm and length $l = 1.25$ mm is used to collect time-series measurements of the streamwise velocity component. A computer-controlled traversing stage is inserted through the top wall of the tunnel along the midpoint of the tunnel span to allow the hot-wire probe to traverse the test section in order to make measurements at different wall-normal y locations. The streamwise position of the hot-wire probe traverse system is adjustable, and the following four streamwise locations are selected for this study: $x = 51$, 102, 170, and 272 mm, which correspond to $1.5\delta_{99}$, $3\delta_{99}$, $5\delta_{99}$, and $8\delta_{99}$, respectively, based on the experimentally measured boundary-layer thickness δ_{99} near the actuator trailing edge. The wall-normal position of the hot-wire probe varies between $y/\delta_{99} = 0.0069$ and $y/\delta_{99} = 0.9724$ for a total of 21 sampling points. The data were sampled at $f_s = 30$ kHz, which corresponds to $\Delta t^+ = (1/f_s)u_\tau^2/\nu = 0.2$ for a total period of 90 s, or about 15,000 δ_{99}/U_∞ in each test. With this sampling frequency and sampling time, there should be no loss of turbulence information as described in Ref. [47].

A plasma-based active large-scale structure actuator (ALSSA) device is used to modify the dynamics of the outer layer of the

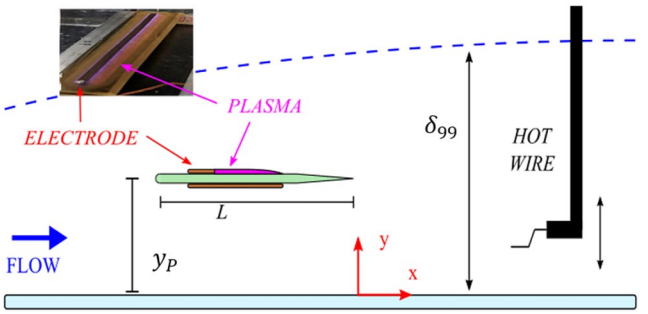

Fig. 2 Schematic of the experimental setup in which an ALSSA comprising a dielectric barrier discharge plasma actuator is mounted on a plate at a prescribed vertical height y_p.

boundary layer with periodic plasma-induced force. This device is attached to the top side of the boundary-layer development plate at a fixed streamwise location of 140 cm from the leading edge of the boundary-layer development plate, as shown in Fig. 2. The plasma actuator is supported above the boundary-layer development plate by vertical, symmetrical NACA0010 airfoils on both sides. These airfoils are 4 mm thick and have a 50 mm wide chord. The plates are made at height intervals y_p at 10 mm ($0.3\delta_{99}$) so that the synthetic large-scale structures can be introduced into the TBL at different heights. The plasma actuator is $W = 25$ cm ($\approx 8\delta_{99}$) wide in the spanwise direction and $L = 32$ mm ($\approx 1\delta_{99}$) long in the streamwise direction. The actuator plate is made of a 2-mm-thick sheet of Ultem dielectric polymer. An upper surface electrode of 0.05-mm-thick copper foil tape is located 15 mm from the plate leading edge and is 4 mm in length and 22 cm in width. On the lower surface, a second copper foil electrode is located 15 mm from the leading edge in line with the top electrode and is 12 mm in length and 22 cm in width. The corners of the electrodes are rounded, and they are mounted in alignment to eliminate extraneous regions of plasma generation and regions of highly concentrated plasma. The leading edge of the actuator plate is rounded, and the last 10 mm of the trailing edge are linearly tapered to reduce the separation region behind the trailing edge of the plate. The alternating current dielectric barrier discharge (ac-DBD) plasma formed on the actuator is produced using a high-voltage ac source consisting of a function generator, power amplifiers, and a transformer [48]. The electrodes placed on the top and bottom of the actuator are connected to the high-voltage ac source, which provides a 40 kV peak-to-peak sinusoidal waveform excitation to the electrodes at a frequency of 4 kHz. The peak-to-peak voltage is maintained within $\pm 5\%$ of the expected excitation voltage during experiments. At the 4 kHz carrier frequency, the plasma actuator operates in a quasi-steady mode, essentially creating a spanwise-uniform steady jet in the streamwise direction. To introduce periodic forcing with frequency f_p, the sinusoidal waveform is modulated by a square wave with a 50% duty cycle. Previous analysis demonstrates that this form of square wave forcing does not produce a significant TBL response at frequencies besides f_p; see, for example, the work by Lozier et al. (Ref. [24], Fig. 3).

The measured velocity time series are then processed by a narrow bandstop filter around 4 kHz to eliminate electronic noise associated with the high-voltage ac source supplying the actuator. Because of the actuator induced periodic forcing of the flow, it is convenient to phase lock the results to the actuation frequency. To do so, a triple phase-locked Reynolds decomposition of the velocity is considered, as shown in Eq. (14a), in which u is the instantaneous velocity; $\bar{u}$ is the time mean component of velocity; $\tilde{u}$ is a phase-locked modal velocity component; u' is a residual fluctuating turbulent component; ϕ is the phase, defined by the relationship in Eq. (14b); and n is the number realizations:

$$u(y,t) = \bar{u}(y) + \tilde{u}(y,\phi) + u'(y,\phi,n) \tag{14a}$$

$$\text{where} \quad \phi = \left(\frac{t_n}{T_p} - n\right)2\pi \tag{14b}$$

Here, t_n is a time in the nth realization, which is related to the phase angle ϕ by the period of the forcing repetition cycle, $T_p = 1/f_p$. The output of the function generator is used to ensure the data are phase locked with the repetition cycle of the plasma. These n realizations are then ensemble averaged to find the modal component of velocity $\tilde{u}(y,\phi)$ as a function of the phase angle.

A set of representative characteristic parameters of the canonical TBL is measured at the downstream location of $x_m = 5\delta_{99}$ using the hot-wire probe. For the canonical turbulent boundary layer used in the experiments, $U_\infty = 7$ m/s, $Re_\theta = 1857$, $\delta_{99} = 34.8$ mm and $H = 1.33$ at the streamwise measurement location $x_m = 5\delta_{99}$. The skin friction velocity u_τ is found using the Clauser method, and the friction Reynolds number is $Re_\tau = 690$. We use this u_τ to normalize all of the experimental results. The inner variable scaled mean velocity and mean square of the streamwise velocity fluctuations of the TBL at $x_m/\delta_{99} = 8$ shown in Fig. 3 demonstrate that the boundary layer exhibits canonical behavior at this location. Additional statistics for this experimental setup are reported in Ref. [49].

B. Model Calibration and Comparison Results

In this subsection, we will describe the forcing model and calibrate the parameters of the forcing function $\check{f}_x$ in Eq. (3) to closely match the effect of the plasma actuation on the flow field. We will then compare the computed results to those obtained from the experimental measurements to demonstrate the efficacy of the spatial input–output analysis method described in Sec. II in reproducing the phase-locked velocity.

Based on the actuator geometry described in Sec. III.A, we model the effect of actuation on the flow by assuming the streamwise body force $\check{f}_x$ in the form of a Gaussian function over the wall-normal direction, a Dirac delta function over the streamwise direction, and a uniform function in the spanwise direction,

$$\check{f}_x(x,y;\omega,k_z) = F_0 \mathrm{e}^{-\frac{(y-y_f)^2}{2\sigma_p^2}} \delta(x - x_0)\mathrm{e}^{\mathrm{i}\phi_0} \tag{15}$$

where F_0 represents the magnitude of this body force and ϕ_0 represents the initial phase induced by the plasma actuator. We select the initial phase of the body force model as $\phi_0 = 1.15\pi$ and the magnitude as $F_0^+ = 38.2$ based on experimental measurements of phase-locked velocity at $x_m = 1.5\delta_{99}$. The values of the parameters ϕ_0 and F_0^+ do not influence the shape of phase-locked velocity due to linearity. In analogy to the vibrating ribbon problem [50] in the study of transitional boundary layers or the signaling problem (see Ref. [39] and Ref. [51]'s Sec. III), the streamwise variation of this body force in Eq. (15) is modeled as a Dirac delta $\delta(x - x_0)$ function over the streamwise direction that is localized at the streamwise position x_0. Here, we impose $x_0 = 0$. The Gaussian function in the wall-normal direction

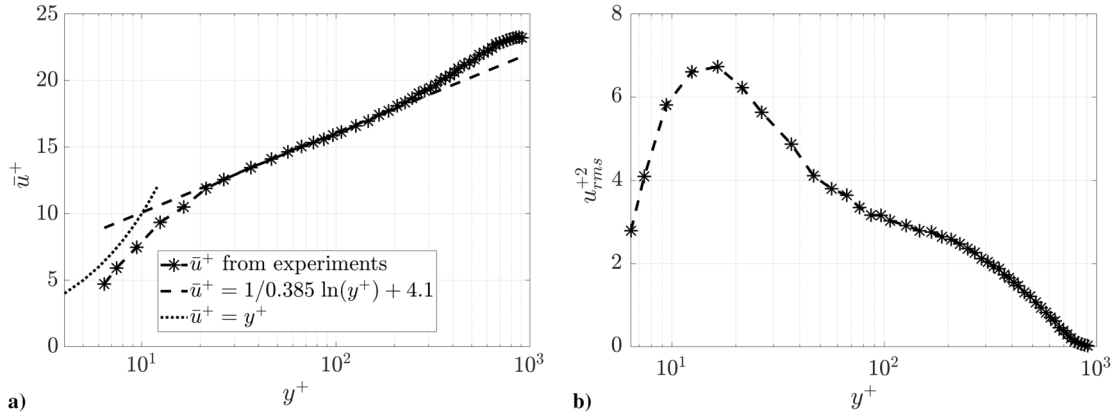

Fig. 3 Experimentally measured a) mean velocity $\bar{u}^+$ and b) mean square of the streamwise velocity fluctuation u_{rms}^{+2} for the canonical turbulent boundary layer at $x_m/\delta_{99} = 8$.

is motivated by Refs. [52,53], where this function is also employed to model localized forcing. The parameters y_f and σ_p in the Gaussian function are, respectively, the center of the peak and standard deviation determining the wall-normal shape of plasma-induced body force. We set $\sigma_p^+ = 60$ and the body force center to be $y_f = 0.13\delta_{99} + y_p$, in other words, $0.13\delta_{99}$ higher than the actuator plate height. This height correction and the standard deviation σ_p^+ of the forcing function are selected in order to match the ALSSA device induced peak phase-locked velocity at $x_m/\delta_{99} = 1.5$ from the experiments. The calibrated values F_0^+, ϕ_0, y_f, and σ_p^+ are then kept constant. The spanwise wave number in Eq. (4) is set to $k_z = 0$ because the plasma actuation in the experiment is spanwise uniform the experimental measurements of flow response do not show significant spanwise variation. We set the frequency to $\omega^+ = 2\pi f_p^+$ to match that of the plasma actuation. We specify the Reynolds number $Re_\tau = 690$ to match the experimental conditions in both the determination of the mean velocity profile and the computations. The actuator plate in the experimental setup will also introduce a wake leading to a velocity deficit in the mean flow, but this wake will decay as the flow continues downstream [25]. The clear peak in the premultiplied streamwise energy spectrum with plasma actuation suggests a much stronger effect of plasma actuation than the actuator plate (see Ref. [49], Fig. 4). We therefore make the simplification of neglecting the effect of the actuator plate and employ the canonical TBL mean velocity profile here. The use of a canonical TBL mean velocity profile does not require experimental measurements to specify the mean profile and provides greater flexibility to explore other flow regimes or actuation schemes. The use of a spatially developing turbulent mean velocity profile requires modifications to the formulation or recalculation at each location of interest and both increase computational time.

The corresponding solution of Eq. (3) at downstream measurement position x_m with respect to the streamwise localized forcing $\check{f}_x$ can be computed using the spatial mapping operator in Eq. (11):

$$\check{\boldsymbol{q}}_S(x_m, y; \omega, k_z) = \check{\boldsymbol{\Psi}}(x_m, x_0, y; \omega, k_z)\check{\boldsymbol{B}}_{S,x}F_0 e^{-\frac{(y-y_f)^2}{2\sigma_p^2}} e^{i\phi_0} \tag{16}$$

To compare with the hot-wire measurements from the experimental setup described in Sec. III.A, we select the streamwise velocity as the output, in other words,

$$\check{u} = \check{\boldsymbol{C}}_{S,u}\check{\boldsymbol{q}}_S \tag{17a}$$

$$\check{\boldsymbol{C}}_{S,u} := \begin{bmatrix} 1 & 0 & 0 & 0 & 0 & 0 \end{bmatrix} \tag{17b}$$

We then obtain the phase-locked velocity defined in (14) at a certain downstream measurement location x_m by multiplying it by $e^{-i\phi}$ to shift the phase,

$$\tilde{u}(x_m, y; \omega, k_z, \phi) = \mathbb{R}e[\check{u}(x_m, y; \omega, k_z)e^{-i\phi}] \tag{18}$$

where $\mathbb{R}e[\cdot]$ represents the real part of the argument. Note that the minus sign in the term $e^{-i\phi}$ in Eq. (18) is based on the fact that an increased phase corresponds to later time moments which is consistent with the phase-locked analysis in Eq. (14) and the ansatz in Eq. (2).

We compare the phase-locked velocity obtained from the proposed spatial input–output analysis against results from experimental measurements associated with an actuation frequency $f_p = 80$ Hz ($0.3983U_\infty/\delta_{99}$ and $f_p^+ = 0.0135$) and an actuator plate height $y_p/\delta_{99} = 0.3$. This actuator plate height $y_p/\delta_{99} = 0.3$ corresponds to the top boundary of the log-law layer [54]. Figure 4 compares the phase-locked velocity obtained from experimental measurements (top panels) and the model (bottom panels) at the four different downstream measurement locations $x_m/\delta_{99} = 1.5$, $x_m/\delta_{99} = 3$, $x_m/\delta_{99} = 5$, and $x_m/\delta_{99} = 8$. In all panels of Fig. 4, the long black dashed line corresponds to the height of the actuator plate y_p, and the short black solid line is the height of the body force center y_f in Eq. (15). Here, we can see that the model provides good qualitative agreement with experimental measurements. At the downstream location $x_m/\delta_{99} = 1.5$, the phase-locked velocity is isolated into three distinct regions across the boundary-layer thickness. We refer to the region below the plate $y/\delta_{99} \in [0, 0.3]$ as the bottom region, the region $y/\delta_{99} \in (0.3, 0.56)$ with y_f in the middle as the central region, and the region $y/\delta_{99} \in [0.56, 1)$ as the top region. As expected, the central region is most strongly influenced by the actuation. The figures indicate that there is a clear phase shift between these regions in both the experimental and model results at all measurement locations. The behavior in the central and top regions is reminiscent of the results from previous studies that showed two similar regions

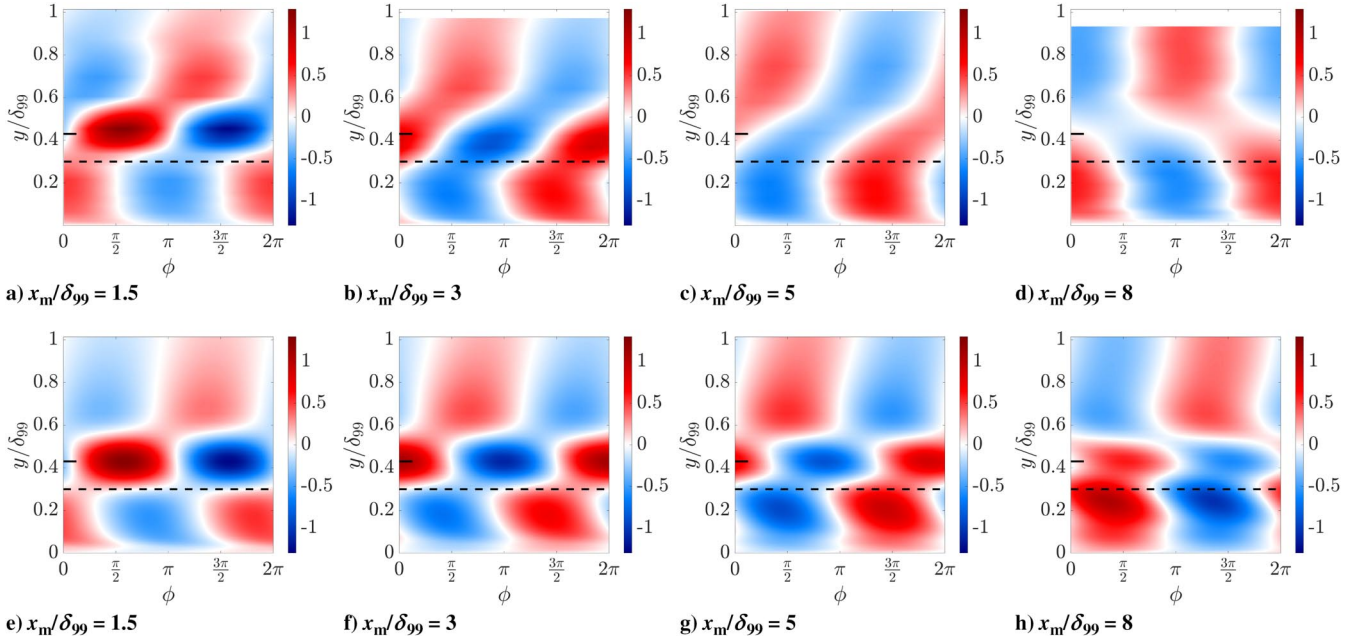

Fig. 4 A comparison of phase-locked modal velocity $\tilde{u}^+$ computed from experiments (panels a–d) using Eq. (14) and that computed from spatial input–output analysis by Eq. (18) (panels e–h) obtained for $y_p/\delta_{99} = 0.3$ and $f_p = 80$ Hz. Here, the long horizontal dashed line (- - -) indicates the plate height of $y_p/\delta_{99} = 0.3$ employed in experiments, and the short horizontal solid line (–) represents the body force center $y_f = y_p + 0.13\delta_{99}$ employed in the body force term described in Eq. (15).

above an actuator (mounted at the wall) [13,17,27,33,34]. The bottom region observed here is not visible in these previous studies [13,17,27,33,34], as their actuation is wall-mounted. The phase-locked velocities in Figs. 4a–4c have a larger phase ϕ at a larger y that is opposite to what is shown in Fig. 4d, which suggests that the direction of phase-locked velocity is changing along the streamwise direction. The results from the model in Figs. 4e–4h captures this phenomenon qualitatively. This behavior is likely due to different phase speeds at different wall-normal heights and suggests the importance of a model that allows a range of streamwise wave numbers. This notion will be examined further in the next section. One of the differences in the spatial input–output results and experimental data is the smoother variation between the top, center, and bottom regions in Figs. 4a–4d versus the sharper interface that appears to occur at a single phase and wall normal height in Figs. 4e–4h. This difference may be due to the choice of a single temporal frequency f_p and single spanwise wave number $k_z = 0$. An interesting direction for future work is the evaluation of the influence of additional temporal frequencies and spanwise wave numbers, which can be introduced by triadic nonlinear interactions; see, for example, Refs. [55,56]. These types of nonlinear effects have also been partially captured in traditional input–output approaches through the addition of an eddy viscosity model (see, for example, Refs. [42–58]), and incorporating such a model into this framework provides another avenue for ongoing investigation.

Figure 5 compares the experimentally measured maximum velocity with the model predicted maximum amplitude of phase-locked velocity $\tilde{u}^+$ in the top, center, and bottom regions for downstream locations $x_m/\delta_{99} = 1.5$, 3, 5, and 8 corresponding to the results in Fig. 4. Here, it is clear that the magnitude of phase-locked velocity $\tilde{u}$ in the central region $y/\delta_{99} \in (0.3, 0.56)$ decays with downstream distance in both the experimental data and model results, although the decay rate of the analytical results is slower, particularly between $x_m/\delta_{99} = 1.5$ and 3. This difference could be a result of the simplified actuator model. This downstream spatio-temporal characteristics of the phase-locked velocity as it decays are consistent with recent work using particle image velocimetry (PIV) measurements to directly track the streamwise evolution of the velocity field [27]. In the top region $y/\delta_{99} \in [0.56, 1)$, the data from the model show a slightly lower maximum value close to the actuator but grow to match the experiment at farther downstream distances. The experimental results show that the magnitude of phase-locked velocity $\tilde{u}$ in the bottom region ($y/\delta_{99} \in [0, 0.3]$) at $x_m/\delta_{99} = 3$ is larger than that at $x_m/\delta_{99} = 1.5$, a trend that is also reflected in the model prediction. The larger phase-locked velocity amplitude below the center of perturbation suggests a spatial transient growth mechanism for the near-wall region. The predicted trend near the wall far downstream of the actuator differs slightly at the two farthest measurement locations $x_m/\delta_{99} = 5$ and 8 as the model predicts a slightly larger maximum, while the experimental results remain relatively constant within the experimental error. The influence of nonlinear interactions between the small scales in the near-wall region is expected to be larger, which may account for the differences.

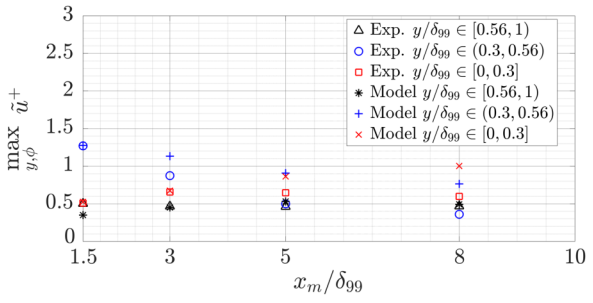

Fig. 5 The experimental measured and model-predicted value of $\max_{y,\phi} \tilde{u}^+$ for the top region $y/\delta_{99} \in [0.56,1)$, the center region $y/\delta_{99} \in (0.3,0.56)$, and the bottom region $y/\delta_{99} \in [0,0.3]$ at downstream locations $x_m/\delta_{99} = 1.5$, 3, 5, and 8 corresponding to results in Fig. 4.

IV. Downstream Propagation of Large-Scale Structures

We next examine the downstream evolution of the streamwise phase-locked velocity; we focus on the streamwise and wall-normal velocity components as the experimental setup leads to a flow that is dominated by the (u, v) velocity in the (x, y) plane and nearly uniform in the spanwise direction due to the spanwise-uniform actuation. To obtain the wall-normal velocity, we modify the output operator as follows:

$$\check{\boldsymbol{v}} = \check{\boldsymbol{C}}_{S,v}\check{\boldsymbol{q}}_S \tag{19a}$$

$$\check{\boldsymbol{C}}_{S,v} := \begin{bmatrix} 0 & 1 & 0 & 0 & 0 & 0 \end{bmatrix} \tag{19b}$$

Based on the experimental configuration, the spanwise vorticity is of primary interest, and this quantity can be obtained as

$$\check{\omega}_z = \check{\boldsymbol{C}}_{S,\omega_z}\check{\boldsymbol{q}}_S \tag{20a}$$

$$\check{\boldsymbol{C}}_{S,\omega_z} := \begin{bmatrix} -\partial_y & ik_x & 0 & 0 & 0 & 0 \end{bmatrix} \tag{20b}$$

We quantify the downstream evolution of the phase-locked velocities for these qualities at each downstream measurement location x_m as

$$u_s(x_m, y; \omega, k_z) = \mathbb{R}\mathrm{e}[\check{u}(x_m, y; \omega, k_z)] \tag{21a}$$

$$v_s(x_m, y; \omega, k_z) = \mathbb{R}\mathrm{e}[\check{v}(x_m, y; \omega, k_z)] \tag{21b}$$

$$\omega_{z,s}(x_m, y; \omega, k_z) = \mathbb{R}\mathrm{e}[\check{\omega}_z(x_m, y; \omega, k_z)] \tag{21c}$$

The experimental measurement of phase-locked velocity is used to construct a pseudospatial evolution of phase-locked streamwise velocity $u_s(x_s, y)$ at the pseudostreamwise location

$$x_s = x_m - \frac{\phi}{2\pi}\frac{1}{f_p}U_c \tag{22}$$

Figure 6 displays the phase speed $U_c^+(x_m, y)$ of the phase-locked velocity associated with the actuation frequency, which is employed to construct the pseudospatial evolution of the phase-locked velocity using Eq. (22). At each wall-normal location y, this $U_c^+(x_m, y)$ is obtained by applying a power law fit between the time-delay of the zero crossing of the streamwise phase-locked velocity and the downstream measurement location x_m. Then, the slope of fitted results at each downstream measurement location x_m and wall-normal location y is employed to obtain $U_c^+(x_m, y)$; for a more detailed description, see Refs. [24,49]. The phase speed of the phase-locked velocity in Fig. 6 asymptotes to a constant value near the wall that is much larger than the turbulent mean velocity. This behavior is qualitatively similar to the convective velocity of large-scale structures observed in the analysis of canonical turbulent channel flow using direct numerical simulation (DNS) data (see Ref. [59],

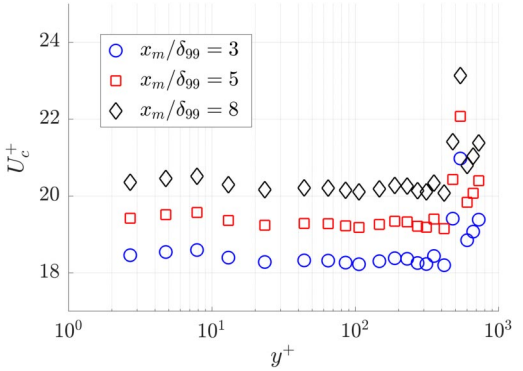

Fig. 6 Phase speed $U_c^+(x_m,y)$ of phase-locked velocity employed to construct pseudospatial evolution of phase-locked velocity.

Figs. 4 and 5) and input–output based methods (see Ref. [60], Figs. 5 and 6). We then extrapolate the hot-wire measurement at $x_m/\delta_{99} = 3$, 5, and 8 upstream for approximately one period using the phase speed $U_c^+(x_m, y)$ in Fig. 6. Near the wall, this corresponds to extrapolating the measurement at $x_m/\delta_{99} = 3$ to obtain $u_s(x_s, y)$ at $x_s/\delta_{99} \in [0.9, 3]$, at $x_m/\delta_{99} = 5$ to obtain $u_s(x_s, y)$ at $x_s/\delta_{99} \in [2.9, 5]$, and at $x_m/\delta_{99} = 8$ to obtain $u_s(x_s, y)$ at $x_s/\delta_{99} \in [5.7, 8]$. When there is any overlap, we perform a linear interpolation using the values at the boundary of the overlap region for a smooth transition between locations. The wall-normal modal velocity $v_s(x_s, y)$ is computed using $u_s(x_s, y)$ and the two-dimensional (x, y)-plane continuity equation.

Figure 7 presents (a) $u_s^+(x_s, y)$ and (b) $v_s^+(x_s, y)$ as a function of pseudostreamwise location x_s and wall-normal height y obtained from experimental measurements. Panels c and d, respectively, show the corresponding computed values from Eqs. (21a) and (21b). Note that the gap in the experimental data near $x_s/\delta_{99} \in [5, 6]$ in Figs. 7a and 7b is because we limit the construction of pseudospatial evolution to one period [see, for example, $u_s^+(x_s, y)$ near $x_s/\delta_{99} = 8$]. We do not extrapolate measurement data to $x_s/\delta_{99} \in [0, 0.9]$, as we expect the phase speed there to vary significantly and the underlying assumption of Eq. (22) to be violated. Here, we note that the values computed using spatial input–output analysis show good qualitative agreement with the experimental measurements at $x_m/\delta_{99} \in [1, 5]$ in terms of both their amplitude and shape over the wall-normal extent. Figure 7c at $x_m/\delta_{99} \approx 8$ also shows a phase shift between the central and top regions compared with $x_m/\delta_{99} \in [1, 5]$, which is consistent with the variation of the experimentally obtained u_s^+ over pseudostreamwise location x_s shown in Fig. 7a. This phase shift observation for both experimental and model based results are consistent with the phase-locked velocity $\tilde{u}^+$ at different downstream locations shown in Fig. 4. This phase shift over the downstream extent can be understood in terms of the difference in the phase speeds over the wall-normal extent. This difference is illustrated through tracking the evolution of a structure in each of the three regions over three periods; this interval is indicated by a dotted line $(\cdots)$ in Fig. 7c. The differences in the locations of these lines clearly illustrate the effect of the wall-normal-dependent phase speed. More specifically, the flow structures in the top region and the central region are traveling slightly faster than those in the bottom region. The shape of the phase-locked velocity observed in Fig. 4 is a direct result of these differences. Changes in the phase speed of the large-scale structures as a function of wall-normal heights have been associated with the stretching and intensifying of the legs of hairpin vortices as they propagate downstream [61]. The results in panels a and c of Fig. 4 highlight the benefit of an analysis method that enables analysis over a wide range of streamwise wave numbers.

The wall-normal velocity v_s^+ obtained from the experimental data and the model are, respectively, shown in Figs. 7b and 7d, which also show good agreement. In contrast to the streamwise component, the v_s^+ computed from experimental data [49] and spatial input–output analysis are nearly uniform across the wall-normal height. Such a nearly uniform wall-normal velocity is consistent with observations in Refs. [13,27] based on planar PIV measurements. Figure 8a presents the spanwise vorticity $\omega_{z,s}^+$ as contours with velocity vectors (u_s, v_s) superimposed. Here, we can see that this body force model generates counterrotating spanwise vorticity near the inflow region. As the actuated large-scale structures propagate downstream, the bottom spanwise vorticity becomes more inclined toward the wall.

Combined information from streamwise and wall-normal velocity can be used to provide insight into the influence of large-scale structures on the Reynolds shear stress. To study this behavior we combine the spatial input–output framework with quadrant analysis [29,30] to classify the shear stress distribution of the spatially evolving flowfield. We then compare the modal structures resulting from actuation with coherent motion in canonical wall-bounded turbulence. The quadrants are defined in terms of the u_s and v_s phase-locked velocities obtained from Eqs. (21a) and (21b). We adopt the traditional definitions for each quadrant; more specifically, the first quadrant Q1 corresponds to outward motions $(u_s > 0, v_s > 0)$, the second quadrant Q2 represents ejections $(u_s < 0, v_s > 0)$, the third quadrant Q3 corresponds to inward motion $(u_s < 0, v_s < 0)$, and the fourth quadrant Q4 behavior corresponds to sweeps $(u_s > 0, v_s < 0)$ [30]. Figure 8b plots regions of the flowfield corresponding to each of these quadrants as a function of streamwise distance in different colors (contours) with the velocity vectors (u_s, v_s) superimposed. Here, the Q4 and Q2 quadrant events are strongest in the central region, particularly close to the actuator $x_m/\delta_{99} \leq 5.5$, while the Q1, Q2, Q3, and Q4 quadrant events appear to be equally distributed throughout the top and bottom regions as well as in the center region farther downstream, i.e., at $x_m/\delta_{99} > 7$. Moving from left to right (along the downstream direction), quadrant events occur in the order

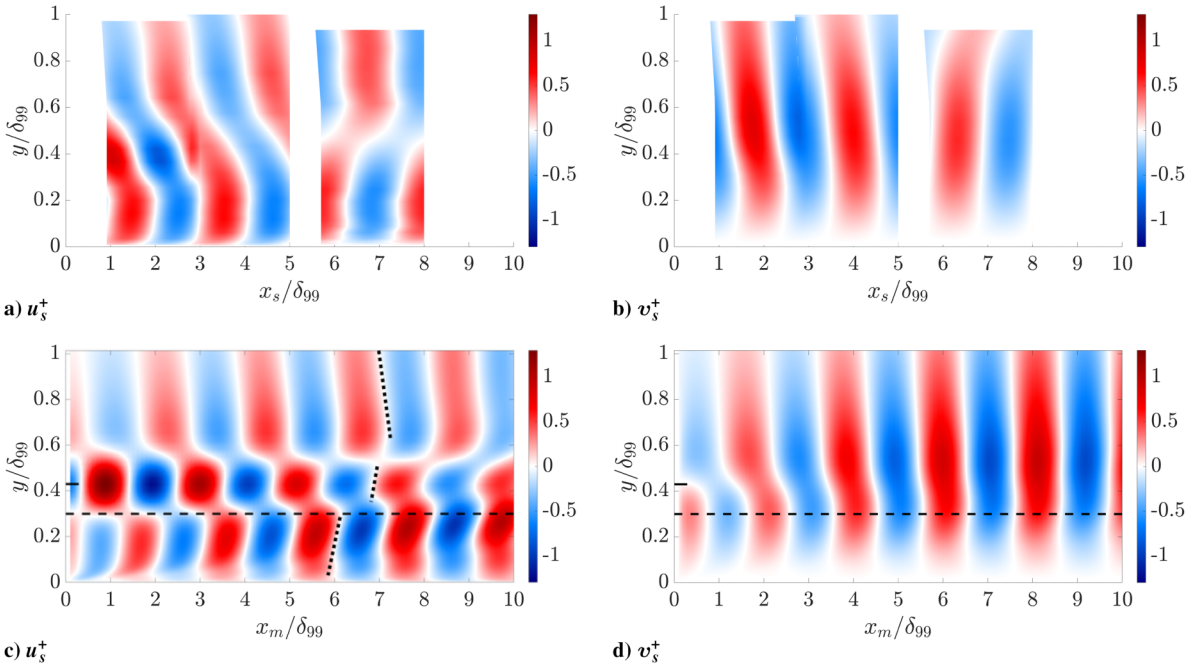

Fig. 7 Downstream evolution of a) u_s^+ and b) v_s^+ from experiments, c) u_s^+ from the model in Eq. (28), and d) v_s^+ from the model in Eq. (29) with $f_p = 80$ Hz, $y_p/\delta_{99} = 0.3$. The dotted line $(\cdots)$ in panel c indicates the downstream distance after three periods. In panels c and d, the long horizontal dashed line (- - -) represents y_p/δ_{99} and the short horizontal solid line (–) indicates $y_f = y_p + 0.13\delta_{99}$.

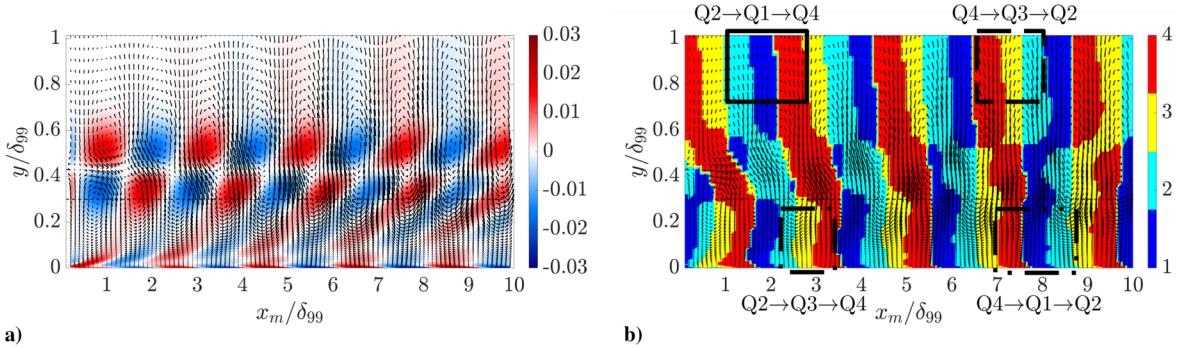

Fig. 8 Contours of a) is spanwise vorticity $\omega_{z,s}^{+}$ and b) quadrant numbers. The velocity vector field (u_s^+, v_s^+) is superimposed on the contours in panels a and b. In panel b, the blue color indicates quadrant Q1, cyan indicates quadrant Q2, yellow corresponds to quadrant Q3, and red denotes quadrant Q4. The boxes with solid line (—), dashed line (- - -), dot-dashed line (-·-), and dot-dot-dashed line (-··-) outline examples of Q2 → Q1 → Q4, Q4 → Q3 → Q, Q2 → Q3 → Q4, and Q4 → Q1 → Q trajectories, respectively.

Q4 → Q3 → Q2 → Q1 in the top region. However, the quadrant event order changes to Q1 → Q2 → Q3 → Q4 in the bottom region. The ordering in both of these regions is consistent with the counterrotating vorticity patterns appearing in the top and bottom regions in Fig. 8a. Quadrant trajectory patterns of Q2 → Q1 → Q4, Q2 → Q3 → Q4, Q4 → Q1 → Q2, and Q4 → Q3 → Q2 were shown to be the most prominent in the dynamics and transport of near-wall turbulence in a previous study that employed quadrant analysis to characterize 36 distinct evolution patterns for (u, v) in turbulent pipe flow [31]. We outline instances of these four important quadrant trajectories using boxes with different line types in Fig. 8b, in which the solid line (—), dashed line (- - -), dot-dashed line (-·-), and dot-dot-dashed line (-··-) boxes, respectively, encompass Q2 → Q1 → Q4, Q4 → Q3 → Q2, Q2 → Q3 → Q4, and Q4 → Q1 → Q2 trajectories. These quadrant trajectories indicate that the interactions of synthetic large scales with the boundary layer are consistent with the dynamics of a canonical TBL, which illustrates the promise of this type of flow interrogation. The ability to perform this detailed study of the downstream evolution and interactions of synthetically generated large-scale structures in actuated TBLs highlights the benefits of spatial input–output analysis.

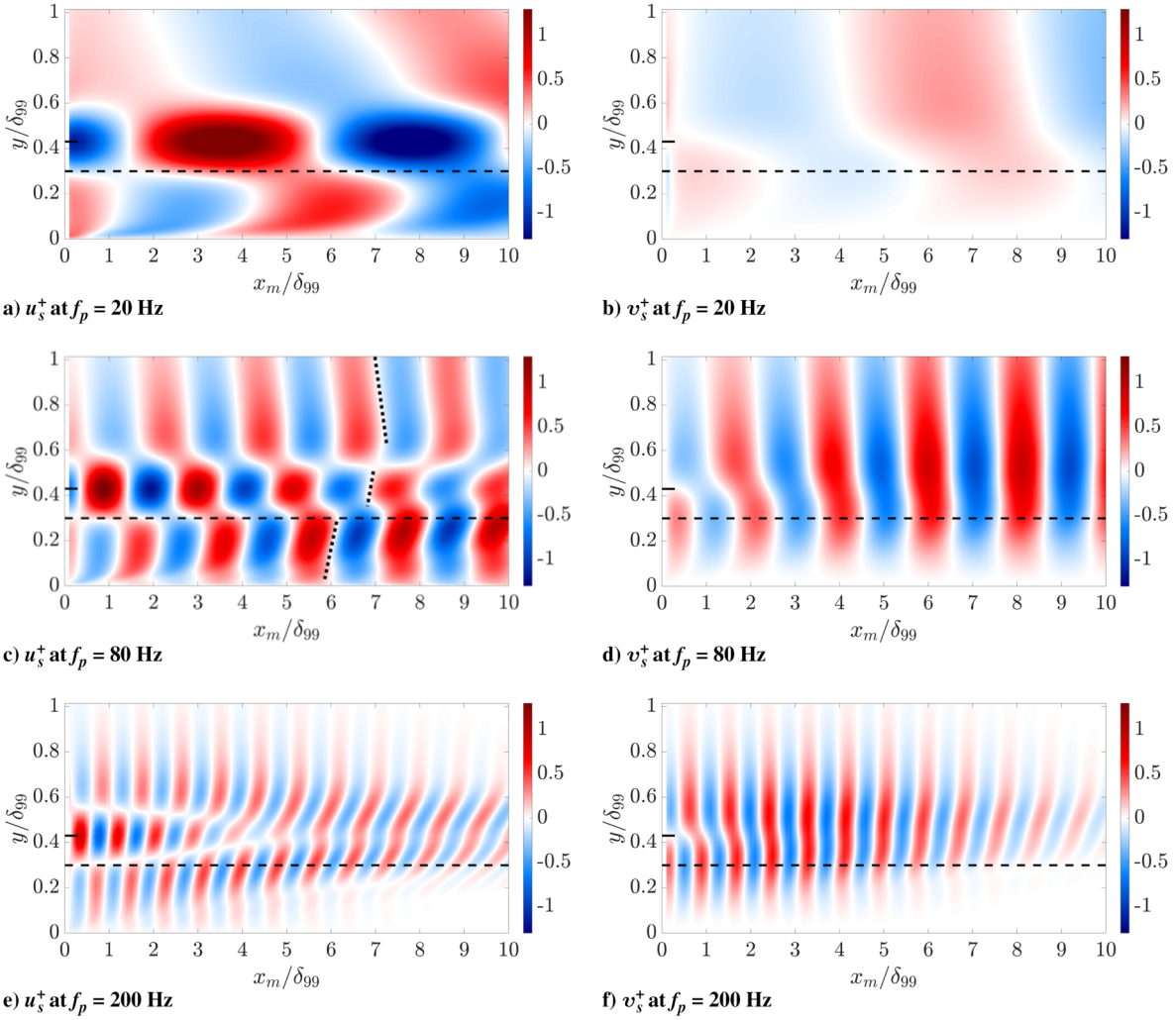

Fig. 9 Downstream evolution of u_s^+ and v_s^+ at $f_p = 20$, 80, and 200 Hz. The plate height is $y_p/\delta_{99} = 0.3$ for all cases. In all panels, the long horizontal dashed line (- - -) marks y_p/δ_{99}, and the short horizontal solid line (–) indicates $y_f = y_p + 0.13\delta_{99}$.

A. Effect of Actuation Frequency and Actuator Height

In this subsection, we employ spatial input–output analysis to study the effect of changes in actuation frequency f_p and actuator plate height y_p. We first investigate the effect of actuation frequency, by introducing two additional frequencies, $f_p = 20$ Hz and $f_p = 200$ Hz, while keeping the plate height fixed at $y_p/\delta_{99} = 0.3$. Then, we analyze the effect of varying the actuator height to values $y_p/\delta_{99} = 0.1$ and $y_p/\delta_{99} = 0.5$ for the fixed actuation frequency $f_p = 80$ Hz.

Figures 9a and 9b show modal velocity components u_s^+, and v_s^+ obtained for an actuation frequency of $f_p = 20$ Hz ($0.0996U_\infty/\delta_{99}$ and $f_p^+ = 0.0034$). These results indicate that the streamwise wavelength of the actuated structures is longer than those in Figs. 7c and 7d, in which the actuation frequency is $f = 80$ Hz, which is consistent with the lower frequency of the actuation. Note, the two modal velocity components for $f = 80$ Hz, from Figs. 7c and 7d are replotted here in Figs. 9c and 9d for ease of comparison. Figures 9e and 9f plot the same quantities as in Figs. 9a and 9b for actuation at $f_p = 200$ Hz ($0.996U_\infty/\delta_{99}$ and $f_p^+ = 0.034$). Here, the large-scale structures show a much smaller streamwise wavelength and decay much faster with downstream distance; see, for example, the streamwise velocity of the central region shown in Fig. 9e. Similar variations with temporal frequencies were observed by Huynh and McKeon [27], who found a linear correlation between temporal frequency and streamwise wave number. We also observe that the flow structures close to the wall at this higher frequency $f_p = 200$ Hz are vanishing at downstream location $x/\delta_{99} \in [7, 10]$ in Figs. 9e and 9f, which suggests that flow structures close to the wall due to off-wall actuation persist for a shorter downstream distance when their streamwise wavelength is smaller. Instead, the flow structures associated with lower frequency in Figs. 9a–9d display longer streamwise wavelength and extend their footprint toward the wall. This behavior is consistent with the observation that large-scale structures associated with large streamwise wavelengths have a footprint that extends farther toward the wall [3,62]. Furthermore, the streamwise velocity at low frequency $f_p = 20$ Hz in Fig. 9a is stronger than that seen in the structures generated by higher-frequency actuation, $f_p = 200$ Hz, in Fig. 9e. Instead, the amplitude of wall-normal velocity for the lower-frequency $f_p = 20$ Hz actuation in Fig. 9b is smaller than that due to the higher-frequency $f_p = 200$ Hz actuation in Fig. 9f. This phenomenon can be qualitatively understood from the two-dimensional continuity equation, which suggests the vertical velocity amplitude is proportional to the streamwise wave number. As shown in Fig. 9, the flow structures associated with $f_p = 20$ Hz possess the largest wavelength (or smallest wave number), leading to the smallest amplitude among these three different frequencies. However, for the high-frequency results ($f_p = 200$ Hz) in Fig. 9f, the spatial transient growth is weaker, and the wall-normal velocity amplitude shows faster downstream decay

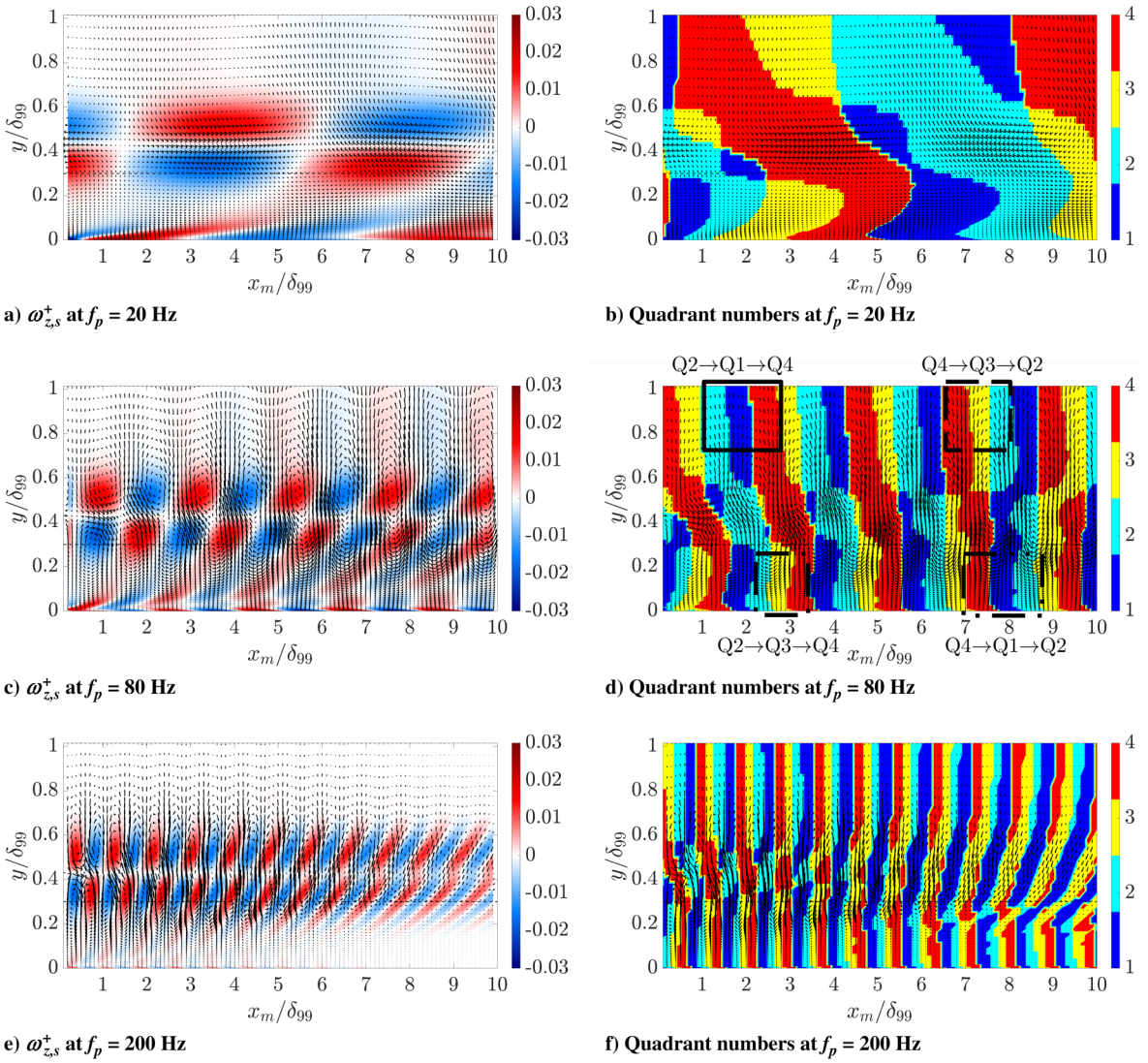

Fig. 10 Downstream evolution of spanwise vorticity $\omega_{z,s}^+$ (a,c,e) and quadrant numbers (b,d,f) at $f_p = 20, 80$, and 200 Hz. All results are associated with $y_p/\delta_{99} = 0.3$. The velocity vector field (u_s^+, v_s^+) is superimposed on the contours. The blue color indicates quadrant Q1, cyan indicates quadrant Q2, yellow corresponds to quadrant Q3, and red denotes quadrant Q4.

compared with the case when $f_p = 80$ Hz. The faster decay leads to vertical velocity amplitudes smaller than that in the data for $f_p = 80$ Hz in Fig. 9d at downstream location $x_m/\delta_{99} \approx 8$. This $f_p = 80$ Hz case displaying the largest wall-normal velocity amplitude also coincides with the frequency leading to the largest modulation coefficient between phase-locked velocity and residual turbulence (see Ref. [25], Fig. 3.10).

Figure 10 shows the spanwise vorticity computed from Eq. (21c) and the results of a quadrant trajectory analysis for the $f_p = 20$ Hz, 80, and 200 Hz cases. For all of these frequencies, the spanwise vorticity in Figs. 10a, 10c, and 10e suggest that the actuated large-scale structures are more inclined toward the wall as they propagate downstream due to their height-dependent phase speed. Comparing the quadrant analysis at actuation frequency $f_p = 20$ Hz, 80, and 200 Hz in Figs. 10b, 10d, and 10f, it is clear that the ejection (Q2) and sweep (Q4) events occupy a larger extent of the (x_m, y) plane at the lowest frequency. This prevalence of Q2 and Q4 events is also observed at $f_p = 80$ Hz (replotted here as Fig. 10d) but is restricted to downstream regions close to the actuator location $x_m/\delta_{99} \lesssim 5$. Table 1 displays the relative prevalence of each quadrant event, computed as $Qi/\sum_{j=1}^{4} Qj$ $(i = 1, 2, 3, 4)$, over the spatial extent $x_m/\delta_{99} \in [0, 10]$ and $y/\delta_{99} \in [0, 1]$. We compute this ratio for each forcing injection height y_p and forcing frequency f_p considered here. The prevalence of Q2 and Q4 events of $f_p = 20$ Hz and $f_p = 80$ Hz with $y_p/\delta_{99} = 0.3$ can be also observed in Table 1 with prevalence ratios greater than 25%.

Close to the actuator $x_m/\delta_{99} \lesssim 2$, the quadrant order at high actuation frequency $f_p = 200$ Hz in Fig. 10f looks similar to the previous analysis at $f_p = 80$ Hz in Fig. 10d, in which the behavior is separated into different vertical bands with alternating Q1 or Q2 quadrant and Q3 or Q4 quadrant (Q1/Q2–Q3/Q4) events. However, farther downstream, the events in Fig. 10f at $f_p = 200$ Hz corresponding to quadrant Q1 and Q3 behavior are more prevalent and stronger than the quadrant Q2 and Q4 events. This larger prevalence of Q1 and Q3 events for $f_p = 200$ Hz is quantified in Table 1, which indicates that both of these types of events occur with prevalence ratios greater than 25%. This can be related to the observation that Q2 and Q4 events are associated with a larger time scale (smaller frequency) than Q1 and Q3 events in fully developed turbulent channel flow [29,30]. An increase in Q1 and Q3 quadrant events is shown to be associated with a negative contribution to Reynolds shear stress; see, for example, Ref. [30]. A reduction in Q2 and Q4 events has also been observed in turbulent

Table 1 Ratio (%) of each quadrant event over all four quadrant events $Qi/\sum_{j=1}^{4} Qj$ $(i = 1,2,3,4)$ occupying the region $x_m/\delta_{99} \in [0,10]$ and $y/\delta_{99} \in [0,1]$ for different actuator heights and frequencies

y_p/δ_{99}	f_p, Hz	$Q1/\sum_{j=1}^{4} Qj$	$Q2/\sum_{j=1}^{4} Qj$	$Q3/\sum_{j=1}^{4} Qj$	$Q4/\sum_{j=1}^{4} Qj$
0.3	20	16.2	34.2	18.0	31.6
0.3	80	20.5	27.9	21.9	29.7
0.3	200	28.9	22.1	28.2	20.8
0.1	80	25.8	24.4	25.3	24.4
0.5	80	18.8	31.0	19.9	30.4

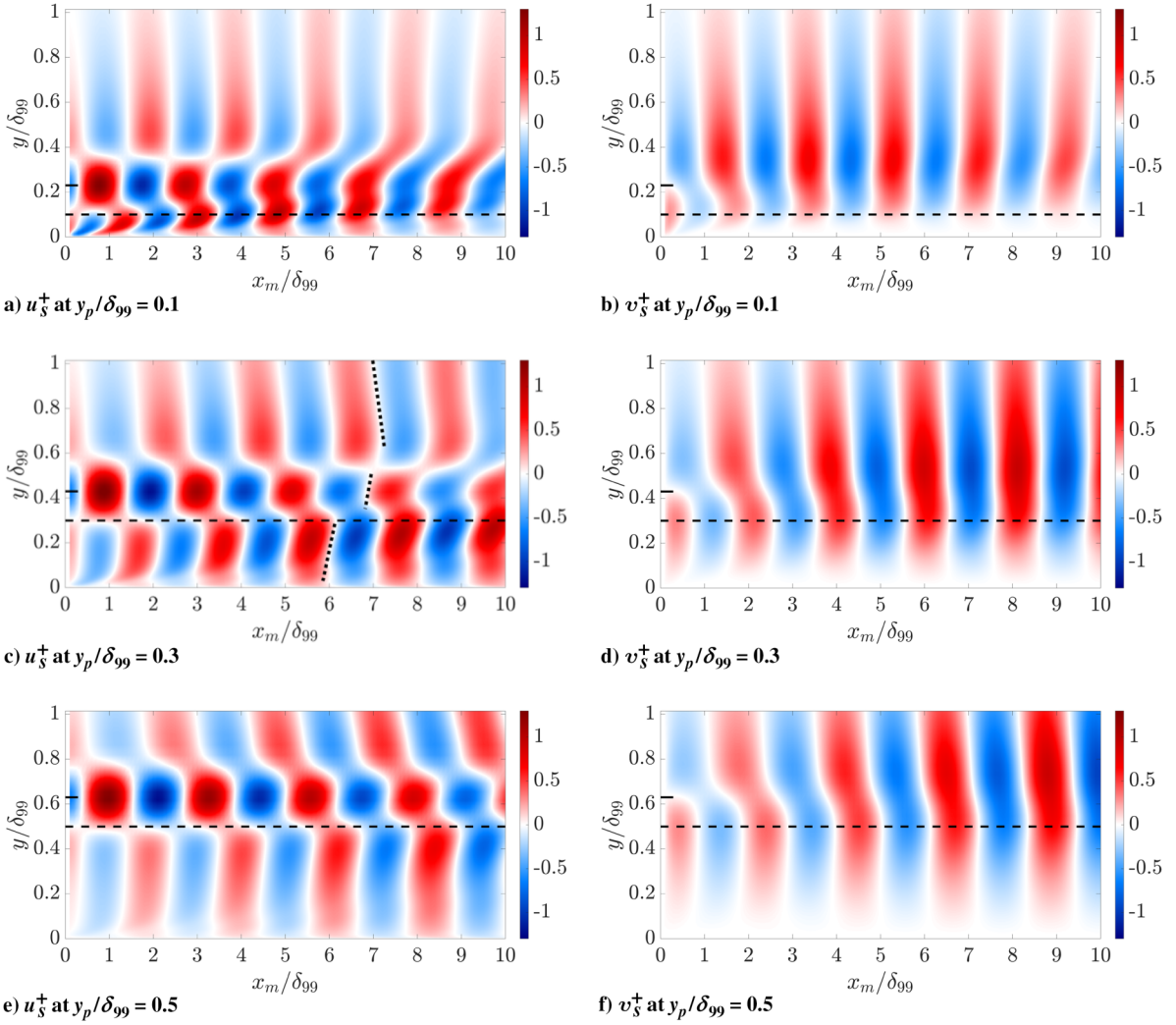

Fig. 11 Downstream evolution of u_s^+ and v_s^+ at $y_p/\delta_{99} = 0.1$, 0.3, and 0.5. All results are associated with $f_p = 80$ Hz. In all panels, the long horizontal dashed line (- - -) marks the location y_p/δ_{99}, and the short horizontal solid line (–) indicates $y_f = y_p + 0.13\delta_{99}$.

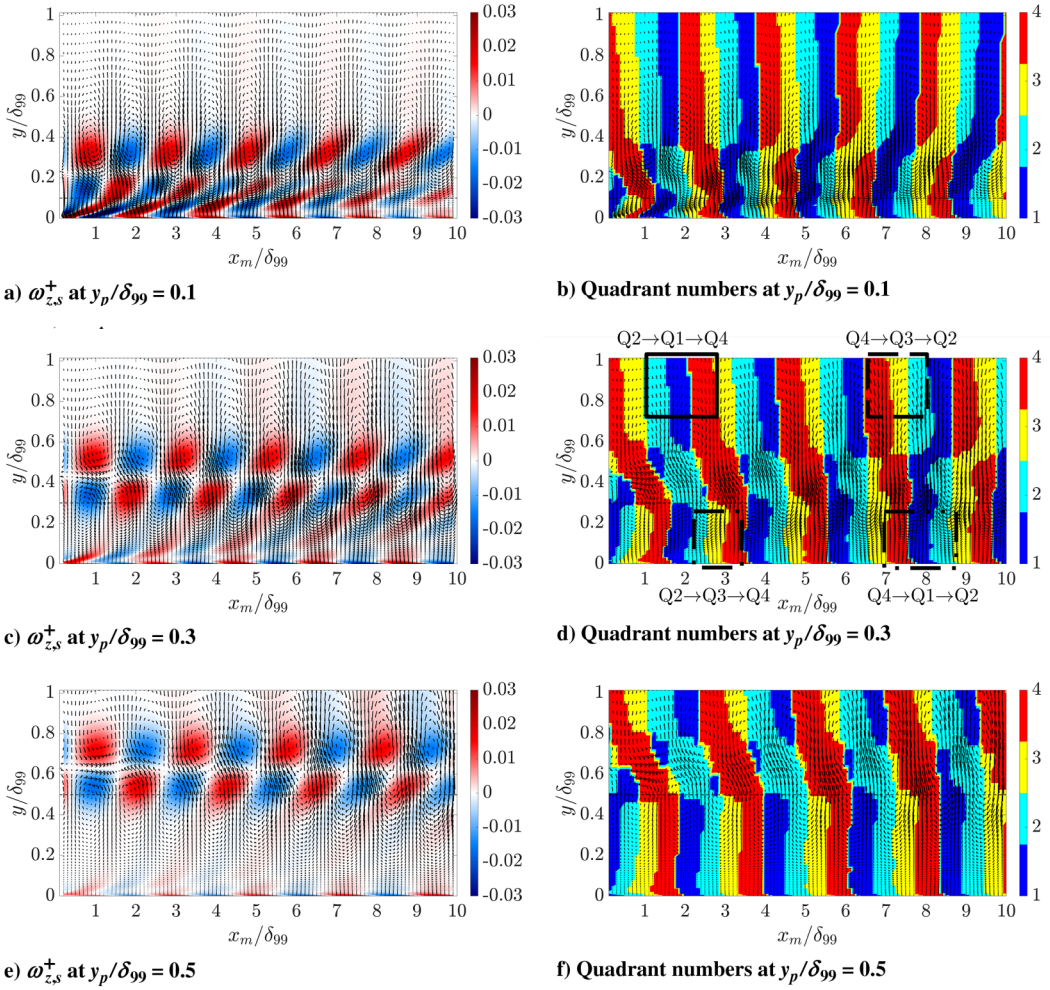

Fig. 12 Downstream evolution of spanwise vorticity $\omega^+_{z,s}$ and quadrant numbers with the velocity vector field (u^+_s, v^+_s) superimposed with $y_p/\delta_{99} = 0.1$, 0.3 and 0.5. The actuation frequency is $f_p = 80$ Hz for all panels. b,d,f) Q1 events are indicated as blue contours, Q2 events are cyan, Q3 events are yellow color, and Q4 events are indicated by red contours.

channel flow with active or passive drag reduction [63,64]. This observation suggests further analyzing the potential to achieve drag reduction by high-frequency actuation, which we leave as a topic of future work. The observation that quadrant events occur in the order Q4 → Q3 → Q2 → Q1 over x in the top region and quadrant events occur in the order Q1 → Q2 → Q3 → Q4 over x in the bottom region is also consistent with important quadrant events characterized in turbulent pipe flow [31].

Finally, we study the effect of different plate heights given a fixed actuation frequency of $f_p = 80$ Hz. Figure 11 shows u^+_s and v^+_s computed for the cases with actuator heights $y_p/\delta_{99} = 0.1$, $y_p/\delta_{99} = 0.3$, and $y_p/\delta_{99} = 0.5$. Comparing the plots of u^+_s in Figs. 11a, 11c, and 11e, it is clear that the characteristic streamwise wavelength is longer when the actuator height is higher. This phenomenon results from a larger phase speed associated with the central region due to a larger local mean velocity at a higher plate height. Here, the effect of differences in phase speed between the central region and bottom region is more visible than in the results for $y_p/\delta_{99} = 0.1$ with $y_p/\delta_{99} = 0.3$. This larger difference is due to the larger mean velocity gradient in the near-wall region. The wall-normal velocity v^+_s generated through actuation at different actuator heights y_p in Figs. 11b, 11d, and 11f shows nearly uniform behavior across the wall-normal height for downstream positions $x_m/\delta_{99} \in [0, 10]$ for all cases.

Figure 12 presents $\omega^+_{z,s}$ and quadrant trajectories associated with actuation at heights $y_p/\delta_{99} = 0.1$, $y_p/\delta_{99} = 0.3$, and $y_p/\delta_{99} = 0.5$. The spanwise vorticity $\omega_{z,s}$ in Figs. 12a, 12c, and 12e indicates similar patterns for all of these actuator heights. The quadrant analysis results in Figs. 12b, 12d, and 12f for these different actuator heights are separated into different vertical bands with alternating Q1 or Q2 quadrant and Q3 or Q4 quadrant (Q1/Q2–Q3/Q4) activity. The quadrant order remains the same as the case with plate height $y_p/\delta_{99} = 0.3$, in other words, Q4 → Q3 → Q2 → Q1 in the top region and Q1 → Q2 → Q3 → Q4 in the bottom region. This suggests that quadrant trajectory orders observed in canonical wall-bounded turbulent flows are robust to the height where the large-scale structures are introduced.

V. Conclusions

This paper uses the one-way spatial integration method of Towne and Colonius [28] to develop a spatial input–output analysis approach that does not require specification of a single streamwise wave number. This approach has the advantage of naturally producing a wall-normal-dependent phase speed allowing the computation of a local convective velocity of the actuated large-scale structures. The paper focuses on the particular problem of a low Reynolds number turbulent boundary layer where a synthetic large-scale structure is introduced through a spanwise-uniform DBD plasma actuator, whose effect is modeled as a streamwise body force associated with a dominant temporal frequency.

The paper first demonstrates that the proposed spatial input–output based analysis produces phase-locked velocities with large-scale structures similar to those obtained by experimental measurements employing hot-wire anemometry and a phase-locked analysis. The authors further predict the decreasing inclination angle of the associated large-scale structures as they propagate downstream, which illustrates the benefit of an analysis method that emits a wall-normal-dependent phase speed. The quadrant analysis used in Refs. [29,30] is applied to classify the shear stress distribution of the spatially evolving flowfield. The results indicate that ordering the field based on

these quadrants produces a trajectory order (Q4 → Q3 → Q2 → Q1 in the top region and Q1 → Q2 → Q3 → Q4 in the bottom region) similar to that observed in turbulent pipe flow [31]. This ordering (spatial progression of quadrant behaviors) is found to be independent of actuator height, while actuator height instead determines a phase speed for flow structures that is close to the local mean velocity at that height. The analysis also captures the relationship between changes in the actuation frequency and the greater prevalence of different shear stress patterns, particularly the association of greater Q2 and Q4 activity with a larger time scale [29]. These observations further support the fact that the synthetic large-scale structures interact with the TBL in a manner consistent with naturally occurring large-scale structures. The analysis therefore suggests that progress in analyzing the dynamics of large-scale structures can be made by studying the effect of introducing external perturbations in a controlled manner.

The results demonstrate that the proposed spatial input–output analysis can provide insights into the large-scale flow structures induced by temporally periodic and spatially localized perturbations in wall-bounded turbulent flows. The method can be naturally extended to study flow structures with spanwise variation by setting $k_z \neq 0$ and spanwise velocity by modifying the output operator. This method may be further extended to analyze flow structures and potential drag reduction induced by more comprehensive actuators by modifying the forcing function and associated input operator following an approach similar to that in [44]. This change would allow the analysis of different types of flow perturbations than the setup considered here.

Appendix: Asymptotic Consistent Turbulent Boundary-Layer Profile

Here, we describe the asymptotic consistent TBL profile developed by Monkewitz et al. [41], which was also used; for example, by Cossu et al. [42]. The mean profile is provided by

$$U = u_\tau[U_i^+(y^+) - U_{\log}^+(y^+) + U_e^+(Re_{\delta_*}) - U_w^+(\eta)] \tag{A1}$$

where u_τ is the wall friction velocity, $y^+ = yu_\tau/\nu$ is the wall-normal location in the inner units, and $U_e^+ = U_e/u_\tau$ is the freestream velocity U_e scaled with u_τ. $Re_{\delta_*} = U_e\delta_*/\nu$ is the Reynolds number scaled on the displacement thickness length scale, and $\eta = y/\Delta$ is the wall-normal coordinate scaled with the Rotta–Clauser outer length scale $\Delta = \delta_* U_e^+$. The inner and the outer coordinates are related by $y^+ = Re_{\delta_*}\eta$. Then, we have the explicit formula for these mean velocities from Ref. [41]:

$$\begin{aligned} U_i^+(y^+) = {} & 0.68285472\,\ell_n(y^{+2} + 4.7673096y^+ + 9545.9963) \\ & + 1.2408249\arctan(0.010238083y^+ + 0.024404056) \\ & + 1.2384572\,\ell_n(y^+ + 95.232690) - 11.930683 \\ & - 0.50435126\,\ell_n(y^{+2} - 7.8796955y^+ + 78.389178) \\ & + 4.7413546\arctan(0.12612158y^+ - 0.49689982) \\ & - 2.7768771\,\ell_n(y^{+2} + 16.209175y^+ + 933.16587) \\ & + 0.37625729\arctan(0.033952353y^+ + 0.27516982) \\ & + 6.5624567\,\ell_n(y^+ + 13.670520) + 6.1128254 \end{aligned} \tag{A2a}$$

$$U_{\log}^+(y^+) = \frac{1}{\kappa}\ell_n(y^+) + B \tag{A2b}$$

$$U_e^+(Re_{\delta_*}) = \frac{1}{\kappa}\ell_n(Re_{\delta_*}) + C \tag{A2c}$$

$$U_w^+(\eta) = \left[\frac{1}{\kappa}E_1(\eta) + w_0\right]\frac{1}{2}\left[1 - \tanh\left(\frac{w_{-1}}{\eta} + w_2\eta^2 + w_8\eta^8\right)\right] \tag{A2d}$$

where $\kappa = 0.384$, $B = 4.17$, $C = 3.3$, $w_0 = 0.6332$, $w_{-1} = -0.096$, $w_2 = 28.5$, $w_8 = 33000$, and $E_1(\eta) = \int_\eta^\infty \frac{e^{-t}}{t}\,dt$. These analytical expressions are validated to be the same as the mean profile at $Re_\tau = 690$ obtained from direct numerical simulations [43,44].[††]

Acknowledgments

The authors gratefully acknowledge support from the Office of Naval Research through grant number N00014-18-1-2534. C. L., I. G., and D. F. G. also acknowledge support from the U.S. National Science Foundation through grant number CBET 1652244. C. L. appreciates the support from the Chinese Scholarship Council.

References

[1] Balakumar, B., and Adrian, R., "Large- and Very-Large-Scale Motions in Channel and Boundary-Layer Flows," *Philosophical Transactions of the Royal Society A: Mathematical, Physical and Engineering Sciences*, Vol. 365, No. 1852, 2007, pp. 665–681. https://doi.org/10.1098/rsta.2006.1940

[2] Guala, M., Hommema, S. E., and Adrian, R. J., "Large-Scale and Very-Large-Scale Motions in Turbulent Pipe Flow," *Journal of Fluid Mechanics*, Vol. 554, May 2006, pp. 521–542. https://doi.org/10.1017/S0022112006008871

[3] Mathis, R., Hutchins, N., and Marusic, I., "Large-Scale Amplitude Modulation of the Small-Scale Structures in Turbulent Boundary Layers," *Journal of Fluid Mechanics*, Vol. 628, June 2009, pp. 311–337. https://doi.org/10.1017/S0022112009006946

[4] Mathis, R., Monty, J. P., Hutchins, N., and Marusic, I., "Comparison of Large-Scale Amplitude Modulation in Turbulent Boundary Layers, Pipes, and Channel Flows," *Physics of Fluids*, Vol. 21, No. 11, 2009, Paper 111703. https://doi.org/10.1063/1.3267726

[5] Marusic, I., McKeon, B. J., Monkewitz, P. A., Nagib, H. M., Smits, A. J., and Sreenivasan, K. R., "Wall-Bounded Turbulent Flows at High Reynolds Numbers: Recent Advances and Key Issues," *Physics of Fluids*, Vol. 22, No. 6, 2010, Paper 065103. https://doi.org/10.1063/1.3453711

[6] Hwang, J., and Sung, H. J., "Influence of Large-Scale Motions on the Frictional Drag in a Turbulent Boundary Layer," *Journal of Fluid Mechanics*, Vol. 829, Oct. 2017, pp. 751–779. https://doi.org/10.1017/jfm.2017.579

[7] Smits, A. J., McKeon, B. J., and Marusic, I., "High-Reynolds Number Wall Turbulence," *Annual Review of Fluid Mechanics*, Vol. 43, No. 1, Jan. 2011, pp. 353–375. https://doi.org/10.1146/annurev-fluid-122109-160753

[8] Abbassi, M., Baars, W., Hutchins, N., and Marusic, I., "Skin-Friction Drag Reduction in a High-Reynolds-Number Turbulent Boundary Layer via Real-Time Control of Large-Scale Structures," *International Journal of Heat and Fluid Flow*, Vol. 67, Oct. 2017, pp. 30–41. https://doi.org/10.1016/j.ijheatfluidflow.2017.05.003

[9] Corke, T. C., and Thomas, F. O., "Active and Passive Turbulent Boundary-Layer Drag Reduction," *AIAA Journal*, Vol. 56, No. 10, 2018, pp. 3835–3847. https://doi.org/10.2514/1.J056949

[10] Hussain, A. K. M. F., and Reynolds, W. C., "The Mechanics of an Organized Wave in Turbulent Shear Flow," *Journal of Fluid Mechanics*, Vol. 41, No. 2, 1970, pp. 241–258. https://doi.org/10.1017/S0022112070000605

[11] Hussain, A. K. M. F., and Reynolds, W. C., "The Mechanics of an Organized Wave in Turbulent Shear Flow. Part 2. Experimental Results," *Journal of Fluid Mechanics*, Vol. 54, No. 2, 1972, pp. 241–261. https://doi.org/10.1017/S0022112072000667

[12] Jacobi, I., and McKeon, B. J., "New Perspectives on the Impulsive Roughness-Perturbation of a Turbulent Boundary Layer," *Journal of Fluid Mechanics*, Vol. 677, June 2011, pp. 179–203. https://doi.org/10.1017/jfm.2011.75

[13] Jacobi, I., and McKeon, B. J., "Dynamic Roughness Perturbation of a Turbulent Boundary Layer," *Journal of Fluid Mechanics*, Vol. 688, Dec. 2011, pp. 258–296. https://doi.org/10.1017/jfm.2011.375

[14] Jacobi, I., and McKeon, B. J., "Phase Relationships Between Large and Small Scales in the Turbulent Boundary Layer," *Experiments in Fluids*,

[††]Data available online at https://torroja.dmt.upm.es/turbdata/blayers/low_re/profiles/ [retrieved 10 February 2020].

Vol. 54, No. 3, 2013, p. 1481.
https://doi.org/10.1007/s00348-013-1481-y
[15] McKeon, B. J., Jacobi, I., and Duvvuri, S., "Dynamic Roughness for Manipulation and Control of Turbulent Boundary Layers: An Overview," *AIAA Journal*, Vol. 56, No. 6, 2018, pp. 2178–2193.
https://doi.org/10.2514/1.J056764
[16] Duvvuri, S., and McKeon, B. J., "Triadic Scale Interactions in a Turbulent Boundary Layer," *Journal of Fluid Mechanics*, Vol. 767, March 2015, p. R4.
https://doi.org/10.1017/jfm.2015.79
[17] Bhatt, S., and Gnanamanickam, E., "Linear and Nonlinear Mechanisms Within a Forced Plane Wall Jet," *Physical Review Fluids*, Vol. 5, No. 7, 2020, Paper 074604.
https://doi.org/10.1103/PhysRevFluids.5.074604
[18] Artham, S., Zhang, Z., and Gnanamanickam, E. P., "Inner–Outer Interactions in a Forced Plane Wall Jet," *Experiments in Fluids*, Vol. 62, No. 2, 2021, pp. 1–20.
https://doi.org/10.1007/s00348-021-03136-4
[19] Tang, Z., Jiang, N., Zheng, X., and Wu, Y., "Local Dynamic Perturbation Effects on Amplitude Modulation in Turbulent Boundary Layer Flow Based on Triple Decomposition," *Physics of Fluids*, Vol. 31, No. 2, 2019, Paper 025120.
https://doi.org/10.1063/1.5083224
[20] Tang, Z., and Jiang, N., "The Effect of a Synthetic Input on Small-Scale Intermittent Bursting Events in Near-Wall Turbulence," *Physics of Fluids*, Vol. 32, No. 1, 2020, Paper 015110.
https://doi.org/10.1063/1.5129042
[21] Tang, Z., Ma, X., Jiang, N., Cui, X., and Zheng, X., "Local Dynamic Perturbation Effects on the Scale Interactions in Wall Turbulence," *Journal of Turbulence*, Vol. 22, No. 3, 2021, pp. 208–230.
https://doi.org/10.1080/14685248.2020.1864388
[22] Ranade, P., Duvvuri, S., McKeon, B., Gordeyev, S., Christensen, K., and Jumper, E. J., "Turbulence Amplitude Amplification in an Externally Forced, Subsonic Turbulent Boundary Layer," *AIAA Journal*, Vol. 57, No. 9, 2019, pp. 3838–3850.
https://doi.org/10.2514/1.J057871
[23] Lozier, M., Midya, S., Thomas, F. O., and Gordeyev, S., "Experimental Studies of Boundary Layer Dynamics Using Active Flow Control of Large-Scale Structures," *Proceedings of the Eleventh International Symposium on Turbulence and Shear Flow Phenomenon*, Southampton, England, U.K., 2019, http://www.tsfp-conference.org/proceedings/2019/330.pdf.
[24] Lozier, M. E., Thomas, F. O., and Gordeyev, S., "Streamwise Evolution of Turbulent Boundary Layer Response to Active Control Actuator," *AIAA Scitech 2020 Forum*, AIAA Paper 2020-0097, 2020.
https://doi.org/10.2514/6.2020-0097
[25] Lozier, M. E., Thomas, F. O., and Gordeyev, S., "Turbulent Boundary Layer Response to Active Control Actuator," *AIAA Scitech 2021 Forum*, AIAA Paper 2021-1455, 2021.
https://doi.org/10.2514/6.2021-1455
[26] McKeon, B. J., and Sharma, A. S., "A Critical-Layer Framework for Turbulent Pipe Flow," *Journal of Fluid Mechanics*, Vol. 658, Sept. 2010, pp. 336–382.
https://doi.org/10.1017/S002211201000176X
[27] Huynh, D., and McKeon, B., "Characterization of the Spatio-Temporal Response of a Turbulent Boundary Layer to Dynamic Roughness," *Flow, Turbulence and Combustion*, Vol. 104, No. 2, 2020, pp. 293–316.
https://doi.org/10.1007/s10494-019-00069-1
[28] Towne, A., and Colonius, T., "One-Way Spatial Integration of Hyperbolic Equations," *Journal of Computational Physics*, Vol. 300, Nov. 2015, pp. 844–861.
https://doi.org/10.1016/j.jcp.2015.08.015
[29] Wallace, J. M., Eckelmann, H., and Brodkey, R. S., "The Wall Region in Turbulent Shear Flow," *Journal of Fluid Mechanics*, Vol. 54, No. 1, 1972, pp. 39–48.
https://doi.org/10.1017/S0022112072000515
[30] Wallace, J. M., "Quadrant Analysis in Turbulence Research: History and Evolution," *Annual Review of Fluid Mechanics*, Vol. 4, 2016, pp. 131–158.
https://doi.org/10.1146/annurev-fluid-122414-034550
[31] Nagano, Y., and Tagawa, M., "Coherent Motions and Heat Transfer in a Wall Turbulent Shear Flow," *Journal of Fluid Mechanics*, Vol. 305, 1995, pp. 127–157.
https://doi.org/10.1017/S0022112095004575
[32] Reynolds, W. C., and Hussain, A. K. M. F., "The Mechanics of an Organized Wave in Turbulent Shear Flow. Part 3. Theoretical Models and Comparisons with Experiments," *Journal of Fluid Mechanics*, Vol. 54, No. 2, 1972, pp. 263–288.
https://doi.org/10.1017/S0022112072000679
[33] Duvvuri, S., and McKeon, B., "Nonlinear Interactions Isolated Through Scale Synthesis in Experimental Wall Turbulence," *Physical Review Fluids*, Vol. 1, No. 3, 2016, Paper 032401.
https://doi.org/10.1103/PhysRevFluids.1.032401
[34] Duvvuri, S., and McKeon, B., "Phase Relations in a Forced Turbulent Boundary Layer: Implications for Modelling of High Reynolds Number Wall Turbulence," *Proceedings of the Royal Society A: Mathematical, Physical and Engineering Sciences*, Vol. 375, No. 2089, 2017, p. 20160080.
https://doi.org/10.1098/rsta.2016.0080
[35] Kotsonis, M., Ghaemi, S., Veldhuis, L., and Scarano, F., "Measurement of the Body Force Field of Plasma Actuators," *Journal of Physics D: Applied Physics*, Vol. 44, No. 4, 2011, Paper 045204.
https://doi.org/10.1088/0022-3727/44/4/045204
[36] Briggs, R. J., *Electron-Stream Interaction with Plasmas*, Massachusetts Inst. of Technology, Cambridge, MA, 1964.
https://doi.org/10.7551/mitpress/2675.001.0001
[37] Schmid, P. J., and Henningson, D. S., *Stability and Transition in Shear Flows*, Vol. 142, Springer Science & Business Media, Berlin, 2012.
https://doi.org/10.1007/978-1-4613-0185-1
[38] Huerre, P., and Monkewitz, P. A., "Local and Global Instabilities in Spatially Developing Flows," *Annual Review of Fluid Mechanics*, Vol. 22, No. 1, 1990, pp. 473–537.
https://doi.org/10.1146/annurev.fl.22.010190.002353
[39] Huerre, P., Batchelor, G. K., Moffatt, H. K., and Worster, M. G., "Open Shear Flow Instabilities," *Perspectives in Fluid Dynamics*, Cambridge Univ. Press, Cambridge, England, U.K., 2000, pp. 159–229.
[40] Weideman, J. A. C., and Reddy, S. C., "A MATLAB Differentiation Matrix Suite," *ACM Transactions on Mathematical Software*, Vol. 26, No. 4, 2000, pp. 465–519.
https://doi.org/10.1145/365723.365727
[41] Monkewitz, P. A., Chauhan, K. A., and Nagib, H. M., "Self-Consistent High-Reynolds-Number Asymptotics for Zero-Pressure-Gradient Turbulent Boundary Layers," *Physics of Fluids*, Vol. 19, No. 11, 2007, Paper 115101.
https://doi.org/10.1063/1.2780196
[42] Cossu, C., Pujals, G., and Depardon, S., "Optimal Transient Growth and Very Large-Scale Structures in Turbulent Boundary Layers," *Journal of Fluid Mechanics*, Vol. 619, Jan. 2009, pp. 79–94.
https://doi.org/10.1017/S0022112008004370
[43] Simens, M. P., Jiménez, J., Hoyas, S., and Mizuno, Y., "A High-Resolution Code for Turbulent Boundary Layers," *Journal of Computational Physics*, Vol. 228, No. 11, 2009, pp. 4218–4231.
https://doi.org/10.1016/j.jcp.2009.02.031
[44] Gluzman, I., and Gayme, D. F., "Input-Output Framework for Actuated Boundary Layers," *Physical Review Fluids*, Vol. 6, No. 5, 2021, Paper 053901.
[45] D'Errico, J., "Eigenshuffle," *MATLAB Central File Exchange*, 2020, https://www.mathworks.com/matlabcentral/fileexchange/22885-eigenshuffle.
[46] Alves, L. D. B., Hirata, S. C., Schuabb, M., and Barletta, A., "Identifying Linear Absolute Instabilities from Differential Eigenvalue Problems Using Sensitivity Analysis," *Journal of Fluid Mechanics*, Vol. 870, July 2019, pp. 941–969.
https://doi.org/10.1017/jfm.2019.275
[47] Hutchins, N., Nickels, T. B., Marusic, I., and Chong, M., "Hot-Wire Spatial Resolution Issues in Wall-Bounded Turbulence," *Journal of Fluid Mechanics*, Vol. 635, Sept. 2009, pp. 103–136.
https://doi.org/10.1017/S0022112009007721
[48] Thomas, F. O., Corke, T. C., Iqbal, M., Kozlov, A., and Schatzman, D., "Optimization of Dielectric Barrier Discharge Plasma Actuators for Active Aerodynamic Flow Control," *AIAA Journal*, Vol. 47, No. 9, 2009, pp. 2169–2178.
https://doi.org/10.2514/1.41588
[49] Lozier, M. E., Thomas, F. O., and Gordeyev, S., "PIV Investigation of the Turbulent Boundary Layer Response to Active Control Actuator," *AIAA Scitech 2022 Forum*, AIAA Paper 2022-0053, 2022.
https://doi.org/10.2514/6.2022-0053
[50] Ashpis, D. E., and Reshotko, E., "The Vibrating Ribbon Problem Revisited," *Journal of Fluid Mechanics*, Vol. 213, April 1990, pp. 531–547.
https://doi.org/10.1017/S0022112090002439
[51] Huerre, P., and Monkewitz, P. A., "Absolute and Convective Instabilities in Free Shear Layers," *Journal of Fluid Mechanics*, Vol. 159, Oct. 1985, pp. 151–168.
https://doi.org/10.1017/S0022112085003147
[52] Jovanović, M., and Bamieh, B., "The Spatio-Temporal Impulse Response of the Linearized Navier-Stokes Equations," *Proceedings of the 2001 American Control Conference*, IEEE Publ., New York, 2001,

pp. 1948–1953.
https://doi.org/10.1109/ACC.2001.946026
[53] Vadarevu, S. B., Symon, S., Illingworth, S. J., and Marusic, I., "Coherent Structures in the Linearized Impulse Response of Turbulent Channel Flow," *Journal of Fluid Mechanics*, Vol. 863, March 2019, pp. 1190–1203.
https://doi.org/10.1017/jfm.2019.15
[54] Pope, S. B., *Turbulent Flows*, Cambridge Univ. Press, Cambridge, England, U.K., 2000.
https://doi.org/10.1017/CBO9780511840531
[55] McKeon, B. J., Sharma, A. S., and Jacobi, I., "Experimental Manipulation of Wall Turbulence: A Systems Approach," *Physics of Fluids*, Vol. 25, No. 3, 2013, Paper 031301.
https://doi.org/10.1063/1.4793444
[56] McKeon, B. J., "The Engine Behind (Wall) Turbulence: Perspectives on Scale Interactions," *Journal of Fluid Mechanics*, Vol. 817, April 2017, p. P1.
https://doi.org/10.1017/jfm.2017.115
[57] Hwang, Y., and Cossu, C., "Amplification of Coherent Streaks in the Turbulent Couette Flow: An Input–Output Analysis at Low Reynolds Number," *Journal of Fluid Mechanics*, Vol. 643, Jan. 2010, pp. 333–348.
https://doi.org/10.1017/S0022112009992151
[58] Hwang, Y., and Cossu, C., "Linear Non-Normal Energy Amplification of Harmonic and Stochastic Forcing in the Turbulent Channel Flow," *Journal of Fluid Mechanics*, Vol. 664, No. 664, Dec. 2010, pp. 51–73.
https://doi.org/10.1017/S0022112010003629
[59] Del Álamo, J. C., and Jiménez, J., "Estimation of Turbulent Convection Velocities and Corrections to Taylor's Approximation," *Journal of Fluid Mechanics*, Vol. 640, Dec. 2009, pp. 5–26.
https://doi.org/10.1017/S0022112009991029
[60] Liu, C., and Gayme, D. F., "An Input-Output Based Analysis of Convective Velocity in Turbulent Channels," *Journal of Fluid Mechanics*, Vol. 888, April 2020, p. A32.
https://doi.org/10.1017/jfm.2020.48
[61] Adrian, R. J., "Hairpin Vortex Organization in Wall Turbulence," *Physics of Fluids*, Vol. 19, No. 4, 2007, Paper 041301.
https://doi.org/10.1063/1.2717527
[62] Saxton-Fox, T., and McKeon, B. J., "Coherent Structures, Uniform Momentum Zones and the Streamwise Energy Spectrum in Wall-Bounded Turbulent Flows," *Journal of Fluid Mechanics*, Vol. 826, Sept. 2017, p. R6.
https://doi.org/10.1017/jfm.2017.493
[63] Choi, H., Moin, P., and Kim, J., "Direct Numerical Simulation of Turbulent Flow Over Riblets," *Journal of Fluid Mechanics*, Vol. 255, Oct. 1993, pp. 503–539.
https://doi.org/10.1017/S0022112093002575
[64] Choi, H., Moin, P., and Kim, J., "Active Turbulence Control for Drag Reduction in Wall-Bounded Flows," *Journal of Fluid Mechanics*, Vol. 262, Oct. 1994, pp. 75–110.
https://doi.org/10.1017/S0022112094000431

Y. Zhou
Associate Editor